Inversion of submesoscale patterns from a high-resolution Solomon Sea model: Feasibility assessment

Lucile Gaultier, Bughsin' Djath, Jacques Verron, Jean-michel Brankart, Pierre Brasseur, Angelique Melet

AGU PUBLICATIONS

JGR

Journal of Geophysical Research: Oceans

RESEARCH ARTICLE

10.1002/2013JC009660

Key Points:
- SST and SSS images contain dynamical submesoscale information
- A Solomon sea model is used to test the inversion method (twin experiments)
- Surface velocity field is corrected using the inversion of tracer images

Correspondence to:
L. Gaultier,
lucile.gaultier@legi.grenoble-inp.fr

Citation:
Gaultier, L., B. Djath, J. Verron, J.-M. Brankart, P. Brasseur, and A. Melet (2014), Inversion of submesoscale patterns from a high-resolution Solomon Sea model: Feasibility assessment, *J. Geophys. Res. Oceans*, *119*, 4520–4541, doi:10.1002/2013JC009660.

Received 27 NOV 2013
Accepted 30 JUN 2014
Accepted article online 4 JUL 2014
Published online 23 JUL 2014

Inversion of submesoscale patterns from a high-resolution Solomon Sea model: Feasibility assessment

Lucile Gaultier[1], Bughsin' Djath[1], Jacques Verron[1], Jean-Michel Brankart[1], Pierre Brasseur[1], and Angelique Melet[2]

[1]CNRS/Université Grenoble Alpes, LGGE, Grenoble, France, [2]Geophysical Fluid Dynamics Laboratory, Princeton University, Princeton, New Jersey, USA

Abstract A high-resolution realistic numerical model of the Solomon Sea, which exhibits a high level of variability at mesoscales and submesoscales, is used to explore new avenues for data assimilation. Image data assimilation represents a powerful methodology to integrate information from high-resolution observations such as satellite sea surface temperature or chlorophyll, or high-resolution altimetric sea surface height that will be observed in the forthcoming SWOT mission. The present study investigates the feasibility and accuracy of the inversion of the dynamical submesoscale information contained in high-resolution images of sea surface temperature (SST) or salinity (SSS) to improve the estimation of oceanic surface currents. The inversion method is tested in the context of twin experiments, with SST and SSS data provided by a model of the Solomon Sea. For that purpose, synthetic tracer images are built by binarizing the norm of the gradient of SST, SSS or spiciness. The binarized tracer images are compared to the dynamical image which is derived from the Finite-Size Lyapunov Exponents. The adjustment of the dynamical image to the tracer image provides the optimal correction to be applied on the surface velocity field. The method is evaluated by comparing the result of the inversion to the reference model solution. The feasibility of the inversion of various images (SST, SSS, both SST and SSS or spiciness) is explored on two small areas of the Solomon Sea. We show that errors in the surface velocity field can be substantially reduced through the inversion of tracer images.

1. Introduction

Over the past few years, the resolution of satellite observation has considerably increased. High-resolution images of sea surface temperature (SST) or chlorophyll have revealed the ubiquitous presence of small-scale filaments in the ocean. Recently, some process studies using very high-resolution idealized models have shown that submesoscale (defined here as scales from 1 to 10 km) dynamics plays an important role in the ocean [*Marchesiello et al.*, 2003, 2011; *Klein et al.*, 2011]. In addition, *Capet et al.* [2008a, 2008b, 2008c] show that the energetic and dynamical roles of submesoscale processes have been largely underestimated. Primary production in the ocean is also largely impacted by submesoscale dynamics. Indeed, modeling studies have shown that primary production is largely underestimated when submesoscale processes are not resolved [*Lévy et al.*, 2001, 2012]. In this context, there is an increasing need to better observe and understand submesoscale dynamics, as well as to represent their impacts on larger scales in ocean numerical models.

Since the 1990s, altimetric satellites have observed the surface ocean dynamic topography. The resulting geostrophic surface currents have provided unprecedented information on the ocean dynamics and surface currents at mesoscales (here characterized by horizontal length scales of 10–100 km) and larger scales. However, such altimetric observations have not yet been able to detect submesoscale signals because of their limited spatial resolution. Recently, the detection of small-scale elongated filaments has been made possible through high-resolution satellite images of SST and of the surface chlorophyll. Such submesoscale features can result from the stirring action of the temperature or chlorophyll fields by the mesoscale activity, for instance during the frontogenesis process [*Thomas et al.*, 2008]. Since high-resolution tracer observations include small-scale structures that have been shaped by the dynamics, these images provide useful information on the surface circulation and can be used to improve the estimate of the surface velocity that is currently obtained from coarser resolution altimetric data. Data assimilation methods aim at improving an estimate using several

sources of information. Thus, the image data assimilation framework has been chosen to study to what extend high-resolution tracer images can be used to enrich the reconstruction of mesoscale velocity fields. Building on *Titaud et al.* [2011], *Gaultier et al.* [2013] (hereafter G2013) have investigated the idea of exploiting and inverting the submesoscale dynamical information contained in satellite tracer fields to improve the representation of ocean currents at meso and larger scales. Their objective is to study the potential of one kind of information, provided by tracer images, to enrich the reconstruction of velocity fields and not to settle a full data assimilation system. However, the robustness and performance of the inversion method could not be verified in their study because no error-free velocity fields are of course available for the real ocean.

In this context, the present study aims at properly evaluating the impact of tracer images on the estimation of the dynamics using the method developed in G2013 and at exploring the potential of image data assimilation at various scales. To assess the accuracy and performance of the method, an idealized framework is needed where the errors in the velocity field (to be corrected through image data assimilation) are perfectly known. Therefore, in the present study, the methodology developed in G2013 is tested using twin experiments from a regional ocean general circulation model (OGCM) of the Solomon Sea. The inversion is performed on two areas using either the information provided by the SST alone, the SSS alone or a combination of both tracers. Then, the contribution of each tracer or combination of tracers to the estimation of the dynamics is assessed.

The regional model used in this study covers the Solomon Sea. The choice of the studied region has been primarily motivated by the investigations that are currently being carried out in the Solomon Sea region under the framework of the South Pacific Circulation and Climate Experiment (SPICE) [*Ganachaud et al.*, 2007, 2008; A. Ganachaud et al., The Southwest Pacific Ocean and Climate Experiment (SPICE), submitted to *Journal of Geophysical Research: Oceans*, 2014].

The Solomon Sea is a relevant region for the objectives of this study since it is a region of intense mesoscale activity [*Gourdeau et al.*, 2014]. Actually, the highest sea level variability of the entire tropical South Pacific ocean are found in the Solomon Sea [*Melet et al.*, 2010b]. In this region of complex topography and intense currents, conditions are propitious for instabilities to develop. For instance, the Solomon Sea western boundary currents undergo strong bathymetric constraints to exit the basin and join the Equatorial Pacific through its narrow straits [*Melet et al.*, 2010b]. Moreover, strong current shears are present both vertically and horizontally in the surface down to thermocline layers [*Cravatte et al.*, 2011; *Melet et al.*, 2013]. Thus, given its natural complexity and its high level of energy, the Solomon Sea represents a region of much interest to test the inversion of meso and submesoscale dynamical information to correct the state of the ocean at larger scales.

As part of SPICE, a high-resolution (1/36°) regional OGCM has been recently developed over the Solomon Sea region [*Djath et al.*, 2014]. The 1/36° resolution should enable a partial representation of submesoscale dynamics ("submesoscale permitting") in this low latitude region where the Rossby radius of deformation, characterizing the scales of mesoscale eddies, is large [*Chelton et al.*, 1998]. Therefore, twin experiments based on a high-resolution simulation of the Solomon Sea provide a suitable benchmark to test the image data inversion method developed in G2013.

The paper is organized as follows. The first section summarizes the image inversion method. In this study, the method is applied on data from the submesoscale permitting realistic model of the Solomon Sea (described in section 3.1), which provides high-resolution tracer image data (presented in 3.2) as well as erroneous velocity fields from which a dynamical image is built (section 3.2). The inversion method, detailed in section 2, is applied to several tracers through various experiments described in section 4, and the amount of dynamical information provided by each tracer to the circulation is estimated (section 5). A summary and conclusions are given in section 6.

2. The Image Inversion Method

The image inversion method is detailed in G2013, only a brief overview is given in this section. To invert the submesoscale information contained in tracer observations and improve the description of mesoscale velocity, the structure information contained in the data is the relevant information. Image data assimilation focuses on the characterization of the structures instead of the pixel values of the image. During the inversion process, two images are considered: an image of the submesoscale filament structures of a tracer such

as SST or SSS and an image of the mesoscale dynamical flow. The objective of the inversion is then to minimize the distance (differences) between these two images.

2.1. The Tracer Image

The first image contains the frontal structures and filaments in the tracers that are shaped by the submeso and mesoscale activity. It is built from the extraction of the contours of the tracer field. More precisely, a normalized gradient of the tracer is computed. Thus, the final image represents filaments shaped by the dynamics. Then, this normalized tracer gradient is binarized (Eq. 1) to keep only the maximum values:

$$\mathcal{I}_{tracer}(i,j) = \begin{array}{ll} 0 & \text{if} \quad ||\nabla \text{tracer}(i,j)|| \leq \sigma \\ 1 & \text{if} \quad ||\nabla \text{tracer}(i,j)|| \geq \sigma \end{array} \tag{1}$$

where i, j are the indices of every image pixel.

The threshold σ is chosen as the 80^{th} percentile in order to keep exactly the largest 20% values of the gradients. This threshold is determined empirically so that the filaments are well extracted in the binarized images. However this threshold may need to be adjusted to the specificities of each study, for example if only a few filaments are present in the tracer image. The binarization process (equation 1) enables us to have the same amount of information in the tracer image and in the image of the dynamical flow (see section 2.2). ||||The process of fronts extraction can be improved by many techniques. First of all, a filter can be applied to reduce noise in the tracer field, then the continuity of filaments can also be rebuilt. Finally, it can be of interest to select fronts by their length and not their strength as strong gradients may overshadow weaker ones. All of these methods have been tested on real observation data (from MODIS sensor). The process of binarization can also be thought over using for example adaptive thresholds. For instance, major gradients could be assigned a value of 1 in the binarized image, while minor gradients could be assigned a weaker value such as 0.5.

In the following, this binarized tracer gradient image is noted $\mathcal{I}_{tracer}$.

2.2. The Dynamical Flow Image: FSLE

The second image contains information on the submeso and mesoscale dynamical flow structures. The transport of tracers in a fluid is strongly linked with dynamical structures that are commonly referred as Lagrangian Coherent Structures (LCS) [*Haller and Yuan*, 2000]. LCS are defined as material curves that exhibit the strongest attraction, repulsion or shearing in the flow over a finite time. A mathematical theory explaining the physical concept of LCS has also been developed in *Haller* [2011] and gives robust criteria to identify repelling and attracting LCS. In a stationary flow, LCS act as barriers and define regions of eddies, stretching or contraction of the fluid. In a time dependent flow, LCS can be detected if the translation velocity of eddies is smaller than the velocity in the eddy, which is generally the case in the ocean. Some Lagrangian tools such as Finite-Size Lyapunov Exponents (FSLE) [*Aurell et al.*, 1997] have been developed to detect LCS in finite time and size data sets. Therefore, in this study, FSLE are used to build an image of the flow that can be compared with the image of tracer filaments. It has indeed been pointed out in several studies that FSLE represent an adequate Lagrangian concept to represent the filaments shaped by the dynamics and detected in tracer observations [*d'Ovidio et al.*, 2004, 2009; *Lehahn et al.*, 2007]. FSLE measures the time t needed to separate particles by a fixed distance [*Aurell et al.*, 1997; *Lacorata et al.*, 2001]. These exponents are computed according to their definition, by the exponential rate at which two particles separate from a distance δ_0 to a distance δ_f:

$$\begin{aligned} \lambda &= \frac{1}{t} ln\left(\frac{\delta_f}{\delta_0}\right) \quad \text{if} \quad \delta_f \quad \text{is reached at} \quad t < T \\ \lambda &= \lambda_{min} = \frac{1}{T} ln\left(\frac{\delta_f}{\delta_0}\right) \quad \text{if} \quad \delta_f \quad \text{is not reached at} \quad T \end{aligned} \tag{2}$$

The parameters in equation 2 are fixed according to *d'Ovidio et al.* [2004]. The initial distance between particles (δ_0) is set to the size of the image pixel. The final distance between particles (δ_f) corresponds to the expected length of the filaments of FSLE. The maximum time of advection of particles is fixed here to $T = 15$ days, which is in-between the advection times of submesoscales (1–10 days) and mesoscales (1 month), and thus enables a good detection of the flow divergence. When the maximum time of advection T is reached, if the distance between particles is smaller than δ_f, then the FSLE takes its minimal value $\lambda_{min} \approx 0.21$ (equation 2).

The computation of FSLE is quite similar to the one developed in G2013. However, the stationarity of the FSLE field cannot be assumed anymore in the present study. Since the model of the Solomon Sea is very energetic, the circulations cannot be assumed stationary. Therefore, the FSLE are computed using the time-evolving velocity fields (nonstationary algorithm). However, the time resolution of the velocity field is degraded to keep only one velocity field every 3 days, which is sufficient to preserve the quality of the FSLE structure, with linear interpolation in time and space. Some studies have shown that fine scale filaments can be computed using FSLE derived from a larger scale flow [*Hernàndez-Carrasco et al.*, 2011]. Indeed, FSLE images derived from mesoscale dynamics reveal submesoscale features that have been shaped by mesoscale velocities. In this study, the use of mesoscale velocity fields is therefore sufficient to compute an image of the flow that contains submesoscale structures. Moreover, as stated previously, FSLE represents the stretching of a fluid and lines of maximum FSLE represent fronts that divide fluid particles coming from a similar region [*Lehahn et al.*, 2007]. Therefore, it does make sense to compare filaments and fronts visible in tracer images with FSLE images.

The FSLE image is binarized using equation 1 so that the filament structures from the binarized FSLE image, $\mathcal{I}_{FSLE}$, can be directly compared to the binarized tracer image $\mathcal{I}_{tracer}$ defined above. In both cases, the percentile σ makes it possible to keep only the lines of maximum FSLE (as can be seen in Figures 8c, 8d, 9c, and 9d in section 5).

2.3. Cost Function

To find the optimal correction to be applied on the velocity field, we introduce a cost function defining the misfit between the image representing the submesoscale flow structures and the image representing the structures in the tracer fields. The optimal velocity field is defined as the one that minimizes the cost function. A first term of the cost function is a measure of the discrepancy between the FSLE image derived from a velocity **u** and the image of the binarized tracer frontal structures (i.e., the binarized norm of the tracer gradient). The second term of the cost function is a background term taking into account the first guess of the velocity. As the computation of the FSLE is not sensitive to the strength of the velocity, keeping information from that first guess is also important to avoid a deviation of the norm of the velocity. For a given velocity field **u**, the cost function can be written as:

$$J(\mathbf{u}) = ||\mathcal{I}_{FSLE}(\mathbf{u}) - \mathcal{I}_{tracer}|| + \mu \mathbf{u} B^{-1} \mathbf{u}^T \tag{3}$$

where μ is a parameter modulating the confidence in the background velocity and B is the background error covariance matrix.

When images from N different tracers are available, the cost function can be generalized as:

$$J(\mathbf{u}) = \sum_{n=1}^{N} \alpha_n ||\mathcal{I}_{FSLE}(\mathbf{u}) - \mathcal{I}_n|| + \mu \mathbf{u} B^{-1} \mathbf{u}^T \tag{4}$$

where α_n are weights representing the confidence in the structure of the filaments derived from the image of the n^{th} tracer, $\mathcal{I}_n$. The weight α_n is not necessarily the same for every tracer image, because all images do not have the same quality; the structure of the filaments may be more or less easily detected for different tracers. Some of the tracers can also be far from being passive tracers, so that the structures may not only be related to advection by the velocity field. Thus, if one image is better than an other one, more confidence can be granted in the corresponding tracer using a large weight α. This weight is chosen empirically in this study but one can think of methods to optimize it automatically, for instance by comparing the variances of the gradient of the tracers or the lengths of the detected filaments.

To find the velocity field **u** giving the most consistent flow with the two images (tracer images and background velocity), the cost function is decreased step by step, using a Monte Carlo method, by picking up a random perturbation (defined in section 4.2) and assessing its relevance using the cost function. Therefore, at each step, the FSLE are computed and compared with the tracer image. To avoid being stuck in local minima, a simulated annealing procedure is employed to decrease the cost function [*Van Laarhoven and Aarts*, 1987]. It consists of accepting the perturbation if the cost function is decreased, or accepting it with a given probability if the cost function is increased. To ensure that the method converges toward a solution,

the amplitude of the perturbation and the probability of acceptance decrease as the solution gets closer to the minimum (see G2013 for more details). Note that the minimum of the cost function should not be null since there is an intrinsic distance between the tracer image and the FSLE image. Therefore, the parameters of the simulated annealing are chosen so that the cost function converges toward the estimated minimum (usually around 0.15). As the solution is not unique (several minima in the cost function), all potential solutions are sampled using a Gibbs Sampler [*Geman and Geman*, 1984; *Casella and George*, 1992] in the vicinity of the minimum of the cost function. The resulting velocity sample stands for the solution of the inversion problem. In the following, to display the result of the inversion, only the velocity field corresponding to the minimum of this sample will be used in the figures. This solution does make sense because the standard deviation of the sample containing all potential solutions is small compared to the corrected velocity.

3. Tools and Data

The objective of this section is to describe the model that is used to perform the twin experiments, and to present the synthetic image data which are obtained from the model simulation.

3.1. High Resolution Model

3.1.1. Description

To assess the image inversion method, submesoscale features need to be at least partially represented in the model solution, knowing that there are currently no realistic model configuration fully resolving ocean submesoscales. For that purpose, the 1/36° resolution regional model on the Solomon Sea is found to be adequate. To obtain ocean model with sufficient resolution, our strategy is to deploy embedded numerical models of the Solomon Sea [*Djath et al*., 2014]: a high-resolution (1/36°) model of the Solomon Sea is interactively nested in a 1/12° model of the tropical southwest Pacific using the AGRIF software [*Debreu et al*., 2008], and the regional 1/12° model of the tropical southwest Pacific is itself embedded offline in a 1/12° global OGCM through open boundaries conditions [e.g., *Tréguier et al*., 2001].

All three models are primitive equations models based on the oceanic component of the Nucleus for European Modelling of the Ocean (NEMO) system [*Madec*, 2008]. The vertical coordinate is geopotential, with 46 levels. The resolution of the vertical grid is finer in the upper ocean (∼6 m) and coarser in the abyss (∼250 m resolution). The bathymetry of the high-resolution Solomon Sea model is based on GEBCO08 data set [*IOC et al*., 2003]. A partial step parameterization is used to improve the representation of the bathymetry. Some processes such as the diffusion and the dissipation of tracers and momentum occur at scales too small to be explicitly resolved in the model and need to be parameterized. The lateral diffusion is performed along isopycnal surfaces with a Laplacian operator whereas the lateral dissipation is achieved along geopotential surfaces using a bilaplacian operator. Vertical diffusivities are calculated using the turbulent closure scheme [*Blanke and Delecluse*, 1993]. Atmospheric fluxes of momentum, heat, and freshwater are diagnosed through classical bulk formulas [*Large and Yeager*, 2009] using the ERA Interim reanalysis [*Dee et al*., 2011].

The regional models were initialized with the climatological mass field of the World Ocean Atlas [*Levitus et al*., 1998] and were integrated from 1989 to 2006. Outputs include daily-averaged tracer (temperature and salinity) and velocity fields.

More details on the model and simulations may be found in *Djath et al*. [2014].

3.1.2. Mesoscale and Submesoscale Activity

The ability of the model to simulate submeso and mesoscale dynamics is first illustrated by examining high-resolution daily-mean fields of the relative vorticity, SST and SSS (Figure 1). The relative vorticity (ζ) field is dominated by mesoscale activity including ocean eddies or isolated vortices, meandering currents, fronts and filaments. Both cyclonic ($\zeta < 0$) and anticyclonic eddies ($\zeta > 0$) are present in the Solomon Sea (see Figure 1a). Around these mesoscale features, submesoscale structures are discernible such as thin, elongated filaments that are a few tens of kilometer wide.

The time-evolution of the relative vorticity field suggests that there is a significant constraint from the bathymetry on the propagation of eddies. Eddies enter the Solomon Sea through its southern open boundary and through its northeastern strait called Solomon Strait (Figure 2d). They can exit the Solomon Sea

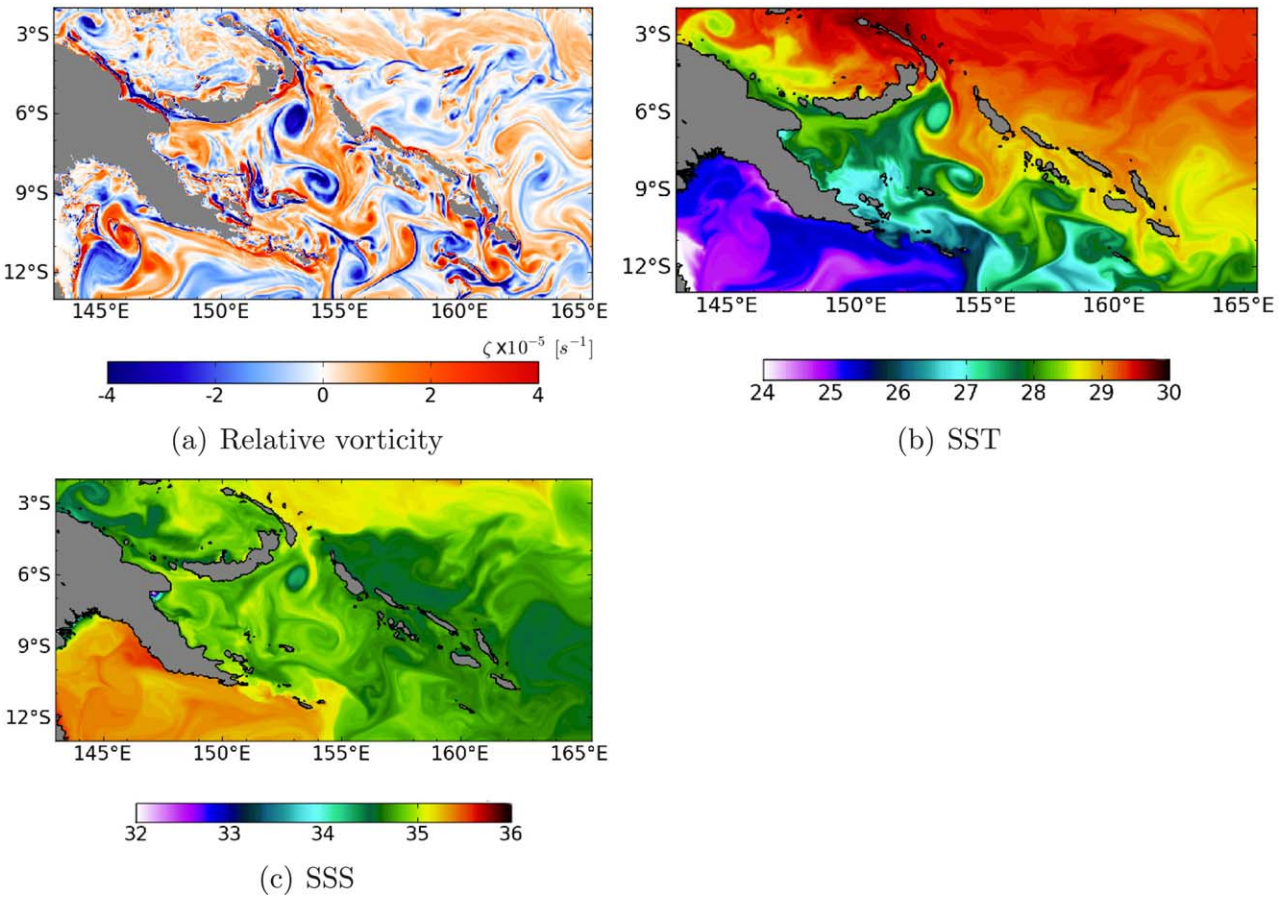

Figure 1. Relative vorticity in (a) s, (b) SST in °C and (c) SSS simulated by the 1/36° Solomon Sea model on 18 July 2000. Cyclonic eddies (blue color) and anticyclonic eddies (red) are revealed in the relative vorticity field.

through its various small straits. An analysis of the mesoscale activity in the Solomon Sea is beyond the scope of this study, but the interested reader is referred to the study of *Gourdeau et al*. [2014].

The dynamical signature of the submeso and mesoactivity can also be clearly identified in the surface tracer images (e.g., the SST and the SSS model outputs, Figures 1b and 1c).

3.1.3. Turbulence and Wave Number Spectrum

Using altimetric data, *Melet et al*. [2010b] showed that in the Solomon Sea, the spatial distribution of the mesoscale activity, as depicted by both sea level variability and eddy kinetic energy (EKE), extends from the north to the south in the midbasin. The highest levels of EKE in the Solomon Sea are found in the northeastern part of the basin, at the mouth of Solomon Strait, with mean values as high as 680 $cm^2\ s^{-2}$. This patch of high EKE is likely associated with barotropic instabilities of the mean flow with the Surface Equatorial Current (SEC) flowing in the Solomon Sea and the LLWBC flowing out of the Solomon Sea.

In the following, EKE and total kinetic energy (TKE) are computed over the entire domain of the Solomon Sea using the high-resolution model and over the 1993–1996 period (Figure 2). The TKE represents the energy contained in currents and the EKE represents the variability of this energy. To characterize the mesoscale activity in the EKE calculation, the daily-mean velocity anomalies are referenced to monthly averaged velocity fields. Consistent with the analysis of altimetric data, the modeled EKE is higher in the eastern part of the basin away from the LLWBCs, and the highest levels are found in the northeastern Solomon Sea (up to 1600 $cm^2\ s^{-2}$, which is equivalent to a rms velocity anomaly of about 40 $cm\ s^{-1}$).

The TKE field exhibits higher levels in the northern than southern part of the Solomon Sea (Figure 2b). The highest TKE values (up to 2000 $cm^2\ s^{-2}$) are found in Vitiaz Strait where most of the Solomon Sea

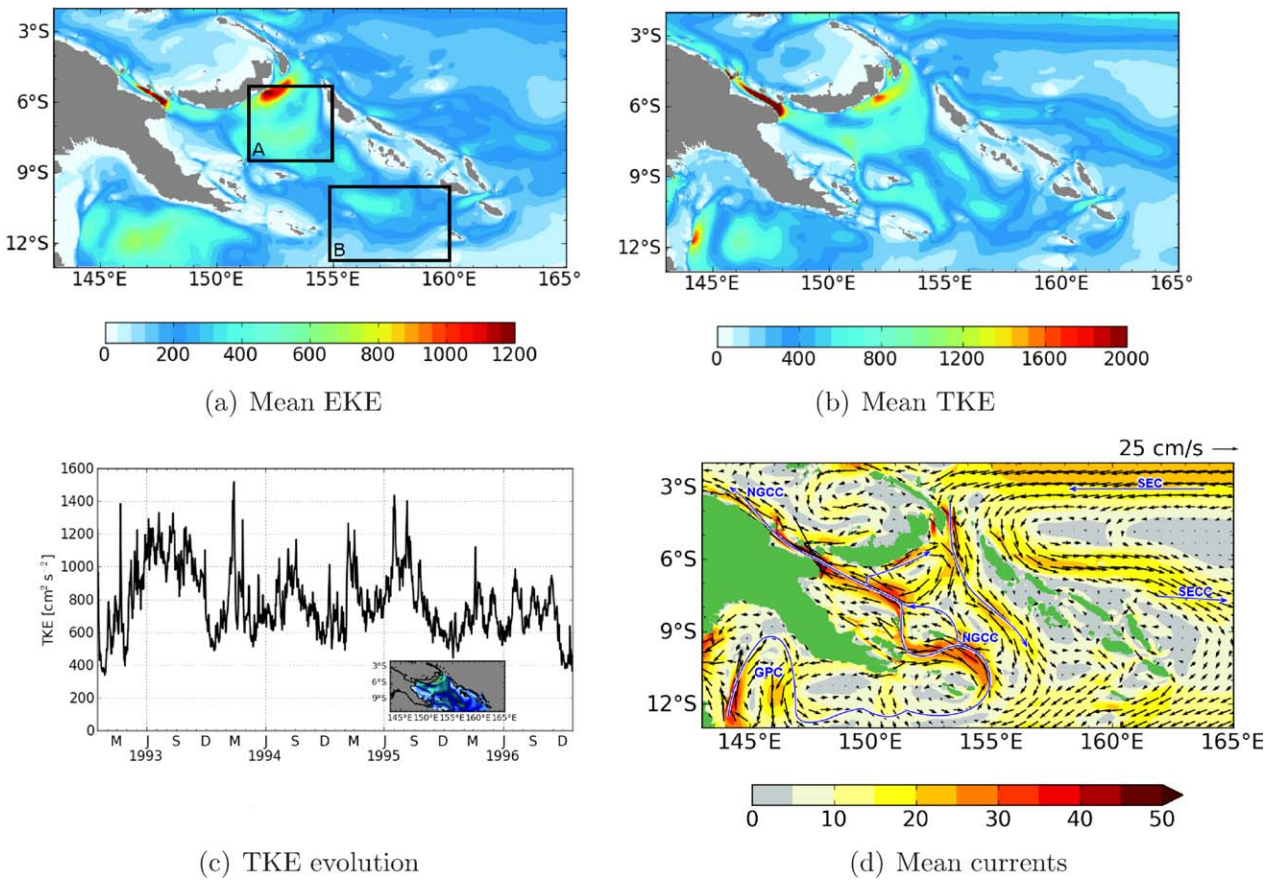

Figure 2. Mean (a) EKE in cm^2s^{-2} and (b) TKE in cm^2s^{-2} from 1993 to 1996. Black squares encompass the regions of high energy (region $\mathbb{A}$) and low energy (region $\mathbb{B}$). (c) Temporal evolution of the TKE averaged over the Solomon Sea (region shown in the subplot) using daily means. (d) Mean surface currents over the 1993–1996 period. The currents amplitudes (shading) are in cm/s. One every 18 vectors are plotted.

equatorward outflow occurs [*Melet et al.*, 2010b; *Cravatte et al.*, 2011; *Hristova and Kessler*, 2011]. The LLWBCs (Figure 1d) have a clear signature on the TKE field, high EKE levels being also associated to high TKE levels. The time series of TKE averaged over the Solomon Sea (Figure 2c) shows that the Solomon Sea is a very energetic region with strong interannual fluctuations. During the period 1993–1996, no strong El Niño event occurred, so the strong signal in TKE for the period 1993–1996 is not a consequence of any particular event but the result of the mesoscale activity in this region.

Based on the spatial heterogeneity of the EKE and TKE fields, two dynamically contrasted areas are selected: (i) one is located in the northeastern Solomon Sea and encompasses the region of high EKE and TKE (area $\mathbb{A}$ in Figure 2a) and (ii) one is located close to the southern boundary of the Solomon Sea and is characterized by low EKE and TKE levels (area $\mathbb{B}$ in Figure 2a). Note that there is a remarkable difference between the two areas: area $\mathbb{A}$ is located in a relatively closed region and is bounded by islands (the Solomon Island chain, New Britain and Papua New Guinea) whereas area $\mathbb{B}$ is a more open oceanic region.

In order to analyze the flow scales, wave number spectra of the sea surface height (SSH) and SST are computed. Such spectra allow to appreciate the way energy is cascading from different spatial scales in the model.

An example of the wave number spectrum of SSH and SST over area $\mathbb{B}$ is shown in Figure 3. These wave number spectra are given as a function of the magnitude of the horizontal wave number. They were obtained by an azimuthal integration in the wave number space. As in the ocean the signals are nonhomogenous and nonperiodic, we first detrend the SSH and SST fields. We then perform spatial Fourier transforms of the fields over the two-dimensional square box in the area $\mathbb{B}$. The fields are made periodic in both the zonal and meridional directions by doubling their size using a mirror symmetry in the zonal and meridional directions as in *Lapeyre* [2009]; *Sasaki and Klein* [2012]. In both spectrum the power spectrum decays

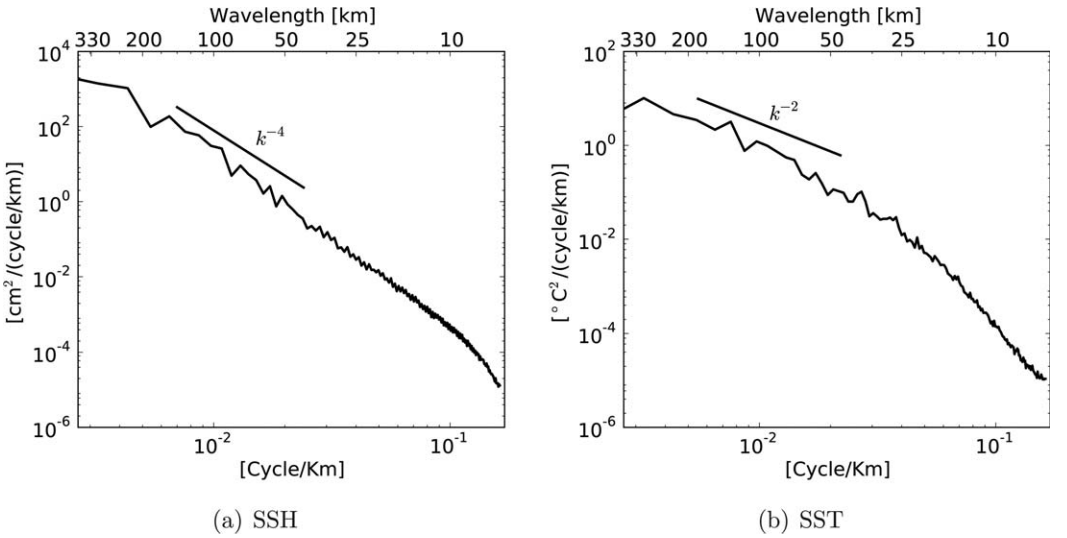

Figure 3. Example of wave number spectrum of (a) SSH and (b) SST on 15 October 1996.

with the wave number: the larger the spatial scales of motion, the larger the associated energy. The slope of the spectrum gives a hint on the dynamics of turbulence in the model. For the mesoscale range ∼25 to 200 km, the slope is in $\approx k^{-2}$ for SST, indicating that surface dynamics is dominated by frontal dynamics [*Sasaki and Klein*, 2012]. The slope of SSH spectrum is in k^{-4}, and the derived kinetic energy spectrum one is in k^{-2}. Consequently, the model turbulence is close to the surface quasi-geostrophic turbulence theory, which is characterized by a nonlinear inverse cascade of total energy (i.e., from small scales to large scales) with a spectral slope in k^{-2} and a cascade toward small scales of the temperature variance with a spectral slope in $k^{-5/3}$ [*Pierrehumbert et al*., 1994].

In this model, the spectra of SSH and SST roll off at scales smaller than approximately 25 km, meaning that the model does not properly resolve ocean dynamics at scales smaller than ∼ 25 km. Therefore, the effective resolution [*Skamarock*, 2004; *Marchesiello et al*., 2011] of the model is closer to 25 km than to 3 km (the resolution of a 1/36° at the latitudes of the Solomon Sea), which is in good agreement with the widely used rule of thumb stating that 8 grid points are needed to properly resolve waves in numerical models. With an effective resolution of ∼ 25 km, the high-resolution model does not properly resolve submesoscale dynamics (characterized by scales of O(1–10) km) but allow submesoscale features to be produced. Therefore, this model cannot be said to be "submesoscale resolving" but is certainly "submesoscale permitting."

In the twin experiments described below, the performance of the inversion will be evaluated over the two dynamically different regions introduced in section 3.1.3. The first case is an inversion using data from region $\mathbb{A}$, a quite energetic area near Solomon Strait. The date of the study is 22 December 1993. Some results from the second test case are also shown, for which the inversion is performed using data from region $\mathbb{B}$ (low energetic region) on 24 September 1995. The dates are chosen to correspond to the presence of an eddy in the area and to be representative of typical dynamical condition in each area.

3.2. Tracer Images

In G2013, the observed SST and surface chlorophyll concentration were used as tracers. Here the method is tested using twin experiments. Observations are therefore synthetic and correspond to outputs from the high-resolution realistic model of the Solomon Sea. The model cannot provide chlorophyll data since it does not include a biogeochemical component so far. The idealized twin experiments framework thus allows us to explore the ability of several tracers to provide relevant dynamical information and to improve the assessment of small scale dynamics. For instance, exploring the inversion of SSS is interesting since SSS contains information at submesoscales and its observation (at coarse resolution) from space started a few years ago with the SMOS/Aquarius mission. From the high-resolution images of SST and SSS, another tracer image can be computed representing the ocean spiciness. Spiciness is density-compensated potential

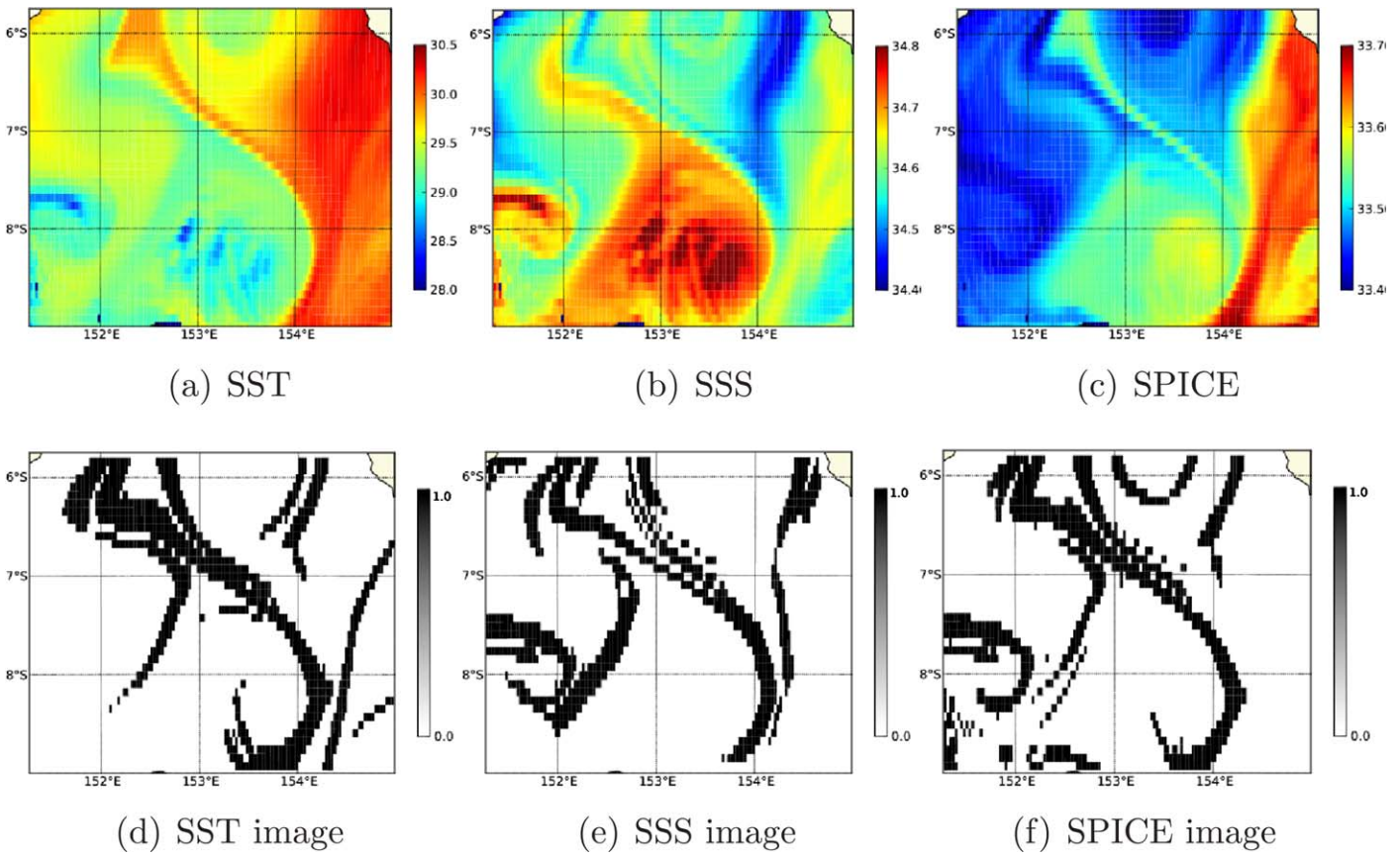

Figure 4. (a) SST in °C, (b) SSS snapshots from the model on 22 22 December 1993, and (c) the corresponding image of spiciness in region $\mathbb{A}$. Binarized norms of the gradient of (d) SST ($\mathcal{I}_{SST}$), (e) SSS ($\mathcal{I}_{SSS}$) and of the spiciness ($\mathcal{I}_{SPICE}$, f) images.

temperature and salinity anomalies [*Veronis*, 1972; *Munk et al*., 1981], with hot and salty waters having high spiciness. For the purpose of our study, spiciness represents an interesting tracer since it mostly behaves as a dynamically passive tracer in the upper ocean [*Klein et al*., 1998]. On the contrary, potential temperature anomalies with a density signature are governed by planetary wave dynamics and behave less passively. Spiciness anomalies found in the Solomon Sea are thought to be produced in the southeastern subtropical Pacific gyre, subducted at thermocline level, and propagated as a dynamically passive tracer by the circulation [*Nonaka and Xie*, 2000; *Yeager and Large*, 2004; *Luo et al*., 2005].

Spiciness is computed as a linear combination of temperature and salinity (equation 5).

$$SPI = \rho_0{}^*(\alpha SST + \beta SSS) \tag{5}$$

where $\alpha = 2.0 \cdot 10^{-4} K^{-1}$ is the thermal expansion coefficient, $\beta = 7.7 \cdot 10^{-4}$ the saline expansion coefficient and $\rho_0 = 1028.5$ an average density.

In region $\mathbb{A}$, frontal structures are clearly revealed in tracer images (Figures 4a–4c), whereas the spatial gradients of the different tracers vary in intensity and the strongest gradients are not located in the same place in each tracer image. Since the binarization of the tracer images only keeps the 20% strongest structures of tracer gradients, filaments that are detected in the SST ($\mathcal{I}_{SST}$) and SSS ($\mathcal{I}_{SSS}$) images are very different (Figures 4d and 4e). This gives evidence of how complementary the structures detected from both images can be. The binarized spiciness image (Figure 4f) is again complementary to that of SST and SSS, with filaments being detected in the spiciness image that are neither in $\mathcal{I}_{SST}$ nor in $\mathcal{I}_{SSS}$. The corresponding fronts are slightly visible in the SST and SSS images (Figures 4a and 4b) but their associated gradients are not strong enough to be detected by the binarization algorithms. The combination of SST and SSS in spiciness makes it possible to detect new fronts.

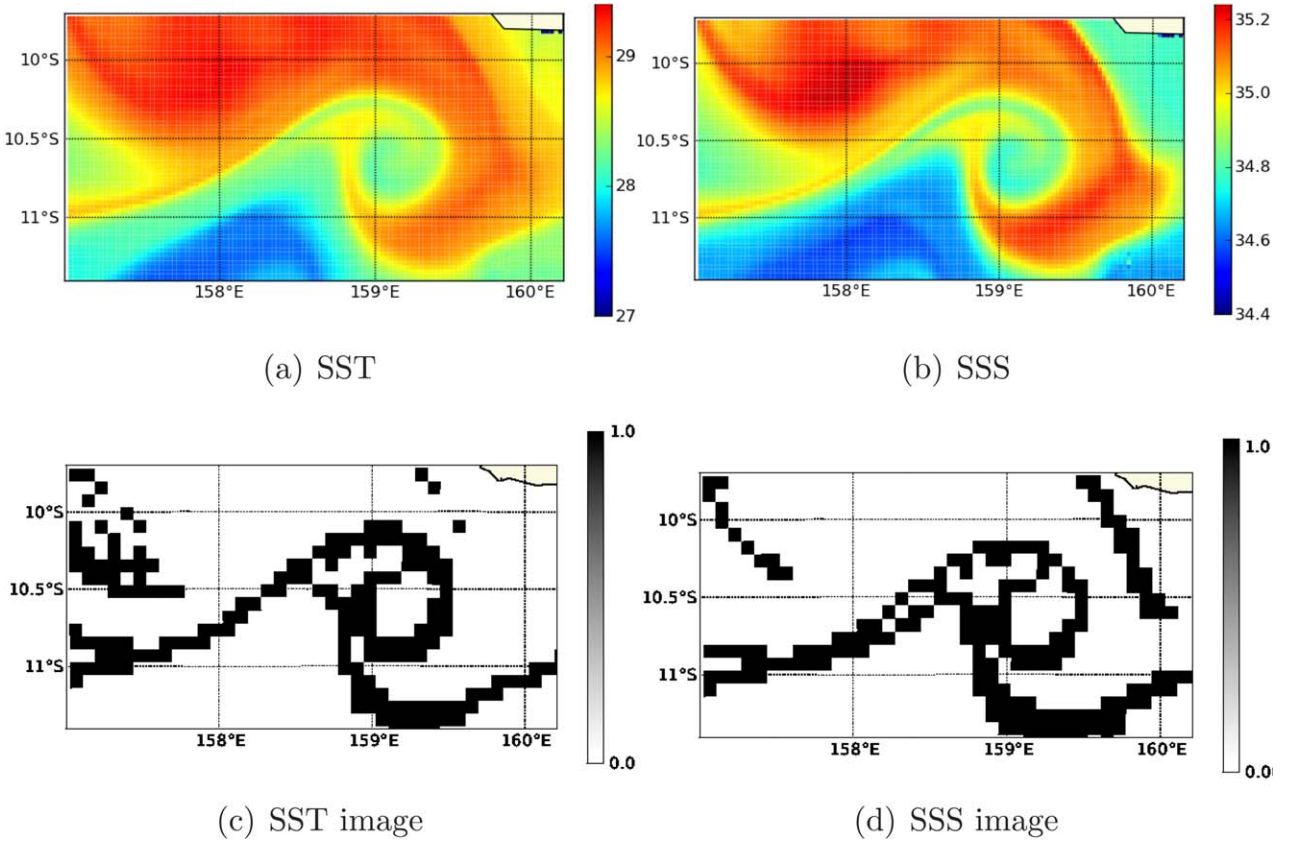

Figure 5. (a) SST in °C and (b) SSS snapshots from the model on 24 September 1993, in region $\mathbb{B}$. Binarized norms of the gradient of the (c) SST ($\mathcal{I}_{SST}$) and (d) SSS ($\mathcal{I}_{SSS}$) images.

As for the second test case, in region $\mathbb{B}$, structures detected from the SST and SSS images are very much alike (Figures 5c and 5d). These two tracers behave more similarly in region $\mathbb{B}$ than in region $\mathbb{A}$. It may be due to the location of the two regions: area $\mathbb{B}$ is located in deeper waters than area $\mathbb{A}$ and may be less influenced by coastal and nonadvective phenomena. As a result, filaments extracted from spiciness (not shown here) are similar to those extracted from SST and SSS. In region $\mathbb{B}$, the computation of spiciness does not provide any additional information.

4. Definition of the Twin Experiments

4.1. True and Background Velocities

Two velocity fields are needed to assess the performance of the inversion process using twin experiments: a true and a background velocity field. The true velocity field is the reference: it is used to evaluate the relevance of the velocity field as estimated by the inversion method. The true velocities (Figures 6a and 7a) are defined as the surface currents that have shaped the filaments in the SST and SSS images. More precisely, the true velocities are the surface velocities (assumed error free) as simulated by the model, on 22 December 1993 (region $\mathbb{A}$), and on 24 September 1995 (region $\mathbb{B}$).

The background velocity field, on the contrary, contains some errors that the inversion of the tracer image aims at reducing. This background velocity field is constructed by adding errors to the true velocity field. The objective is to generate errors with an amplitude similar to that expected in the velocity field deduced from altimetric observations. In the present study, the background velocity is obtained using model velocity before the date of the inversion (22 December 1993 or 24 September 1995). In this way, most eddies present in the true velocity field are also present in the background velocity, but their location is shifted and their shape is slightly altered (see Figure 6 for experiment $\mathbb{A}$ and Figure 7 for experiment $\mathbb{B}$). This kind of error is expected in altimetric observations because of their limited time and space resolution.

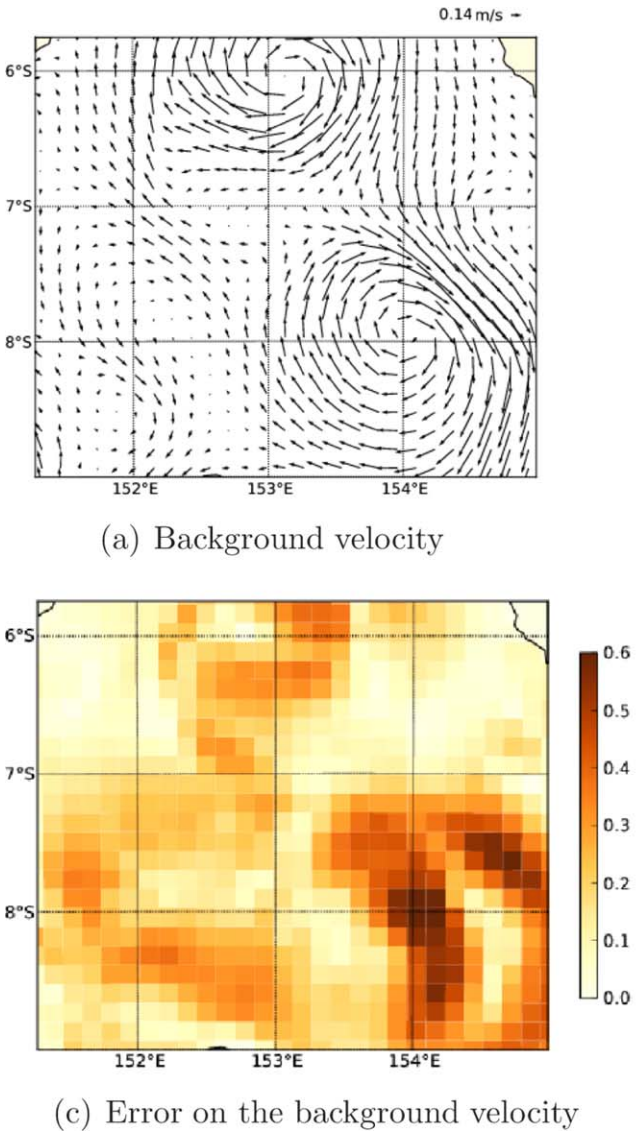

Figure 6. (a) True velocity, (b) background velocity, and (c) norm $\ell 2$ of the difference between the true velocity and the background velocity in ms^{-1} for the experiment on region $\mathbb{A}$.

In this study, the velocity field is degraded to 1/12° resolution for the computation of FSLE since, as mentioned previously, the latter does not require a very high-resolution velocity field to exhibit small scale features [*Hernàndez-Carrasco et al*., 2011]. For example, using data from the Solomon Sea model, one can verify that the main features derived from the 1/36° resolution velocity are still present if FSLE are computed using the velocity filtered at a 1/12° resolution. It is also easier to use a degraded velocity since fewer grid points are considered in the inversion process and need to be corrected. More precisely, the velocity fields used hereafter are derived from the 1/36° model velocities by applying a Lanczos low-pass filter degrading the resolution from 1/36° to 1/12°.

4.2. Error Subspace

The third piece of information that is needed for the inversion is an appropriate description of the background error covariance matrix *B*, which must be consistent with the error introduced on the background velocity. Thus, using velocity fields available in the model seems appropriate to generate the error subspace. In addition, for the inversion to be practically feasible, it is also required that the rank of *B* is small enough, for instance by reducing *B* to its first few eigenvectors. To build this low rank matrix *B* matching

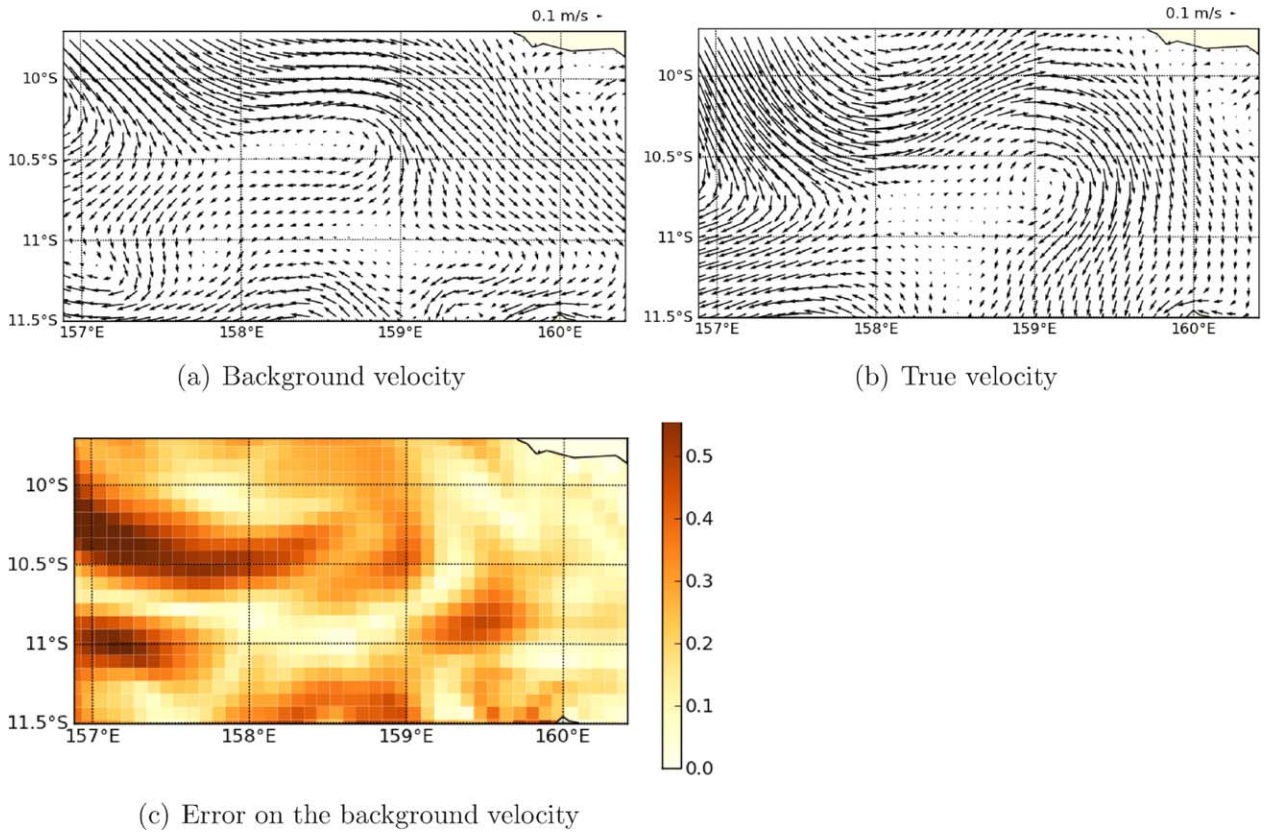

Figure 7. (a) True velocity, (b) background velocity, and (c) norm $\ell 2$ of the difference between the true velocity and the background velocity in ms^{-1} for the experiment on region $\mathbb{B}$.

the amplitude of the error on the background velocity, an ensemble representing the variability of the velocities during 5 day periods is generated. As the Solomon Sea model is very energetic and its variability is significant (section 3.1), the real matrix B contains many directions of error that need to be included in the error subspace. Moreover, to simplify the problem and avoid getting lost in too many dimensions, only a limited size ensemble of velocity fields is used to build the matrix B. Several ensemble sizes have been tested to tune the matrix B during the inversion of FSLE images (see section 5.2), and the ensembles have been constructed differently for region $\mathbb{A}$ and $\mathbb{B}$, as their dynamical behaviors are very different. To build the error subspace, the following subset of model velocity fields is selected:

$$\Delta\mathbf{u}=\mathbf{u}(k)-\mathbf{u}(k+5), k \in [D-49, D] \tag{6}$$

with D the day at which the inversion is performed (22 December 1993 for region $\mathbb{A}$ and 24 September 1995 for region $\mathbb{B}$). Only the 50 velocity fields corresponding to the daily averaged model outputs of the 50 days preceding the inversion date are considered to build the ensemble. Then an EOF analysis is performed on this subset of 50 Δu, and the corresponding 50 EOFs define the reduced rank matrix B. During the inversion, this error subspace is explored, looking for the velocity among the linear combination of the 50 EOFs ($S_1 \ldots S_{50}$). Thus, the velocity perturbation $\delta\mathbf{u}$ can be written:

$$\delta\mathbf{u}=\sum_{n=1}^{n=50} x_n S_n \tag{7}$$

where x_n are random coefficients. It should be noted that the construction of the matrix B is quite idealized here since it is assumed that the statistics of the model simulations are known. To explore the ability and performance of the inversion method based on different tracer images, using a quite idealized matrix B is not a

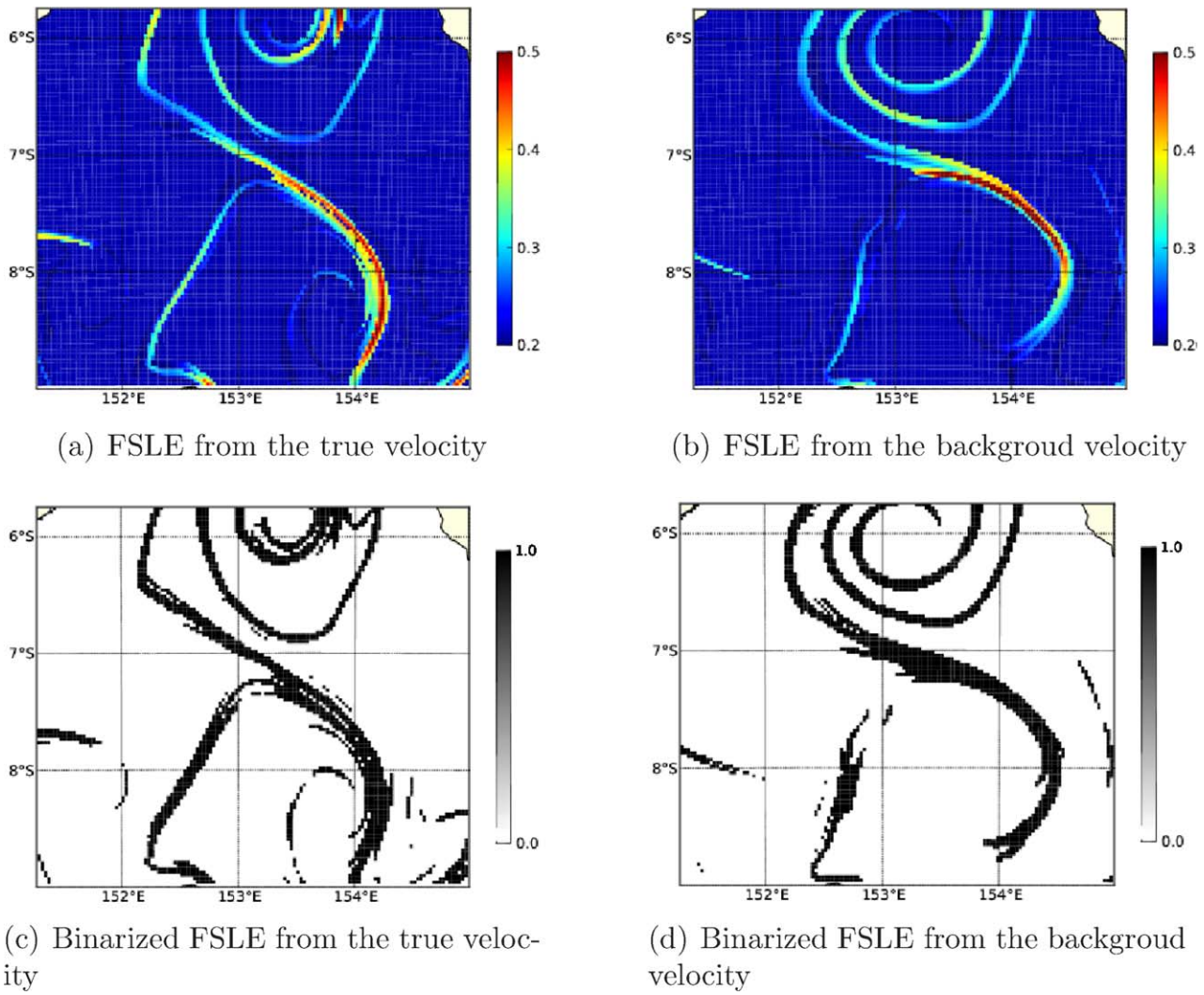

Figure 8. FSLE (in days), computed using the (a) true velocity and (b) background velocity for region $\mathbb{A}$. Binarized FSLE, computed using the (c) true velocity and (d) background velocity.

major concern. In our study, such an idealized matrix B is sufficient since the relative efficiency of the inversion of several tracer images is to be assessed and not the performance of the method in general. However, building a suitable background error covariance matrix for a real data assimilation problem may be more challenging.

4.3. Experiments

The inversion method is tested and evaluated using different tracers. In the following, four experiments are performed and analyzed in which the background velocity field is corrected using filamental structures from:

1. SSS image in experiment 1
2. SST image in experiment 2
3. both SSS and SST images in experiment 3
4. Spiciness image in experiment 4

When the inversion is performed using only one tracer image, the cost function is defined as in equation 3, with $\mathcal{I}_{tracer}$ the binarized norm of the gradient of either the SST image (in experiment 1), the SSS image (in experiment 2) or the spiciness image (in experiment 4).

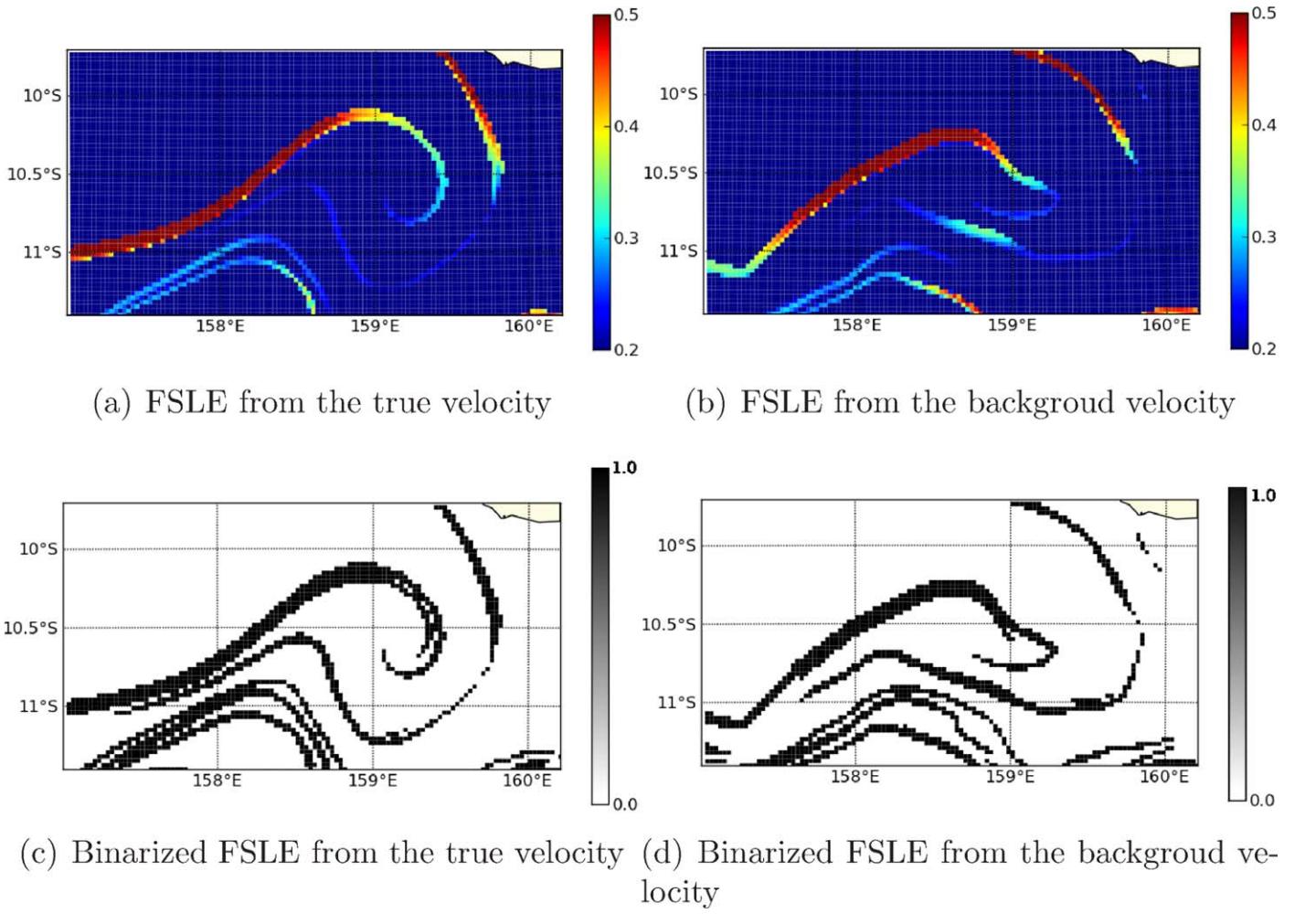

(a) FSLE from the true velocity (b) FSLE from the backgroud velocity

(c) Binarized FSLE from the true velocity (d) Binarized FSLE from the backgroud velocity

Figure 9. FSLE (in days), computed using the (a) true velocity and (b) background velocity for region $\mathbb{B}$. Binarized FSLE, computed using the (c) true velocity and (d) background velocity.

In experiment 3, two tracer images are used, and the corresponding cost function is detailed in equation 4. $\mathcal{I}_{tracer1}$ is the binarized norm of the gradient of the SST image and $\mathcal{I}_{tracer2}$ is the binarized norm of the gradient of the SSS image. As the extraction of filaments are as good in the SST as in the SSS image (section 3.2), the weights are set to be identical for both tracers ($\alpha_{SST}= \alpha_{SSS}= 0.5$ in equation 4).

As the measure of the distance between a tracer image and the FSLE image is strongly nonlinear (because of the binarization of the frontal structures), experiments 3 and 4 can provide different results. Indeed, in experiment 3, the sum of the distance between the FSLE and the binarized SST fronts with the distance between the FSLE and the binarized SSS fronts is minimized whereas in experiment 4, the distance between the FSLE and the binarized fronts of the linear combination of the SST and the SSS is minimized.

5. Results

The data and methodological frameworks presented previously are used to investigate the performance of the inversion process.

5.1. Validity of FSLE as a Proxy

First, the FSLE are computed from the true and background velocities in regions $\mathbb{A}$ (Figures 8a and 8b) and $\mathbb{B}$ (Figures 9a and 9b). Note that to compute the FSLE corresponding to the background velocity, the past velocities are assumed to be known so that the background FSLE is derived from true model velocities from

the past plus the background velocity of the study date. The FSLE image contains information from true velocities from the past, but as only one velocity every 3 days is considered during the computation, the FSLE derived from the background velocity still differs from the FSLE derived from the true velocity (Figures 8a, 8b, 9a, and 9b). As mentioned earlier, the lines of maximum gradients of tracers and the lines of maximum FSLE are expected to be in good agreement even though tracers are not truly passive tracers in the ocean. On the one hand, FSLE represent the stretching of the fluid. Thus, the lines of maximum FSLE are shaped by various instabilities such as the fronts that separate fluid particles coming from similar region [*Haller*, 2011; *Shadden et al*., 2005; *Mathur et al*., 2007]. On the other hand, tracers in a fluid are advected by the flow, and their distribution is shaped by the currents. Thus, tracers tend to develop fronts along the unstable manifold, where velocities are convergent [*Lehahn et al*., 2007]. The spatial gradients of the tracer are therefore perpendicular to the frontal structures, and mostly correspond to the unstable manifold.

In practice, even if SST and SSS are not passive tracers, they still contain information that can be inverted to correct the circulation. An additional difficulty occurs if the tracer is too homogeneous over the domain of study, as the presence of gradients in the tracer is needed to extract the structures. Some discrepancies between the binarized FSLE image ($\mathcal{I}_{FSLE}$) and the binarized norm of the gradient of the tracer ($\mathcal{I}_{tracer}$) can also arise because of the binarization process. Indeed, if the gradients detected in the tracer image are not strong enough, they no longer appear in the binarized image where only the strongest gradients are kept.

As we have access to the true velocity and to the corresponding tracer in the model, tracer frontal structures can be compared with lines of maximum FSLE and the similarity between the two quantities can be corroborated. A qualitative comparison shows that in region $\mathbb{A}$, the spiciness image (Figure 4f) provides frontal structures that are more similar to the corresponding FSLE (Figure 8c), whereas some discrepancies are found between the frontal structures provided by the SST or the SSS (Figures 4d and 4e) and the true FSLE (Figure 8c) in regions where the gradients are not distinctive enough. This means that spiciness may give a more appropriate image to detect the dynamical structure of the flow. The result of the inversion of spiciness should be better than those of the inversion of the SST or the SSS alone. In region $\mathbb{B}$, the frontal structures in both images ($\mathcal{I}_{SST}$ and $\mathcal{I}_{SSS}$) are very similar to the one obtained in the corresponding FSLE (Figure 9c). Generally speaking, information on the dynamics from tracers are often complementary and the use of several tracers during the inversion is usually beneficial to the estimation of the circulation.

A more quantitative diagnostic is now presented to compare the FSLE and tracer binarized images. Similarly to *Lehahn et al*. [2007], the angle between the line of maximum gradient in the tracer and the line of maximum FSLE is measured. The lower the angle, the more similar the structures in the two binarized images are. Histograms of the angles between fronts in the FSLE computed with the true velocity and fronts in the binarized SSS image are presented in Figure 10 in both regions (results from the SST and spiciness images are similar). Nearly a third of the angles are below 10° and more than half of them are below 20°, meaning that lines of maximum FSLE match lines of maximum gradients of the tracer. Note that all histograms have been computed in the model for every day of the 1993–2000 period and they are all very similar to the one shown in Figure 10. The interquartile of the computed angles is also of interest to evaluate the absolute dispersion. In this model it is generally lower than 8, which means that the angles are very similar (50% of the angles are separated by less than 8°). We can thus conclude from this model that even though SST and SSS are not passive tracers and contain only partial information on the dynamics, comparing them with the FSLE in the Solomon Sea region does make sense.

5.2. Feasibility of FSLE Inversion

The first requirement for the image inversion to be successful is that the FSLE proxy to the image is itself invertible. In other words, a necessary condition is that the velocity field can be retrieved from the FSLE proxy. To check that the FSLE inversion is successful, the cost function is minimized using the FSLE computed from the true velocity instead of the tracer image.

The velocity field inferred from the inversion of the binarized true velocity FSLE image is very close to the true velocity (not shown). Therefore, the velocity can be retrieved from the corresponding FSLE. This kind of analysis is also helpful to optimize the different parameters of the inversion process (such as μ, the confidence on the background velocity or parameters concerning the simulated annealing) as well as to check that the selected error subspace is adequate for the inversion without having access to the truth.

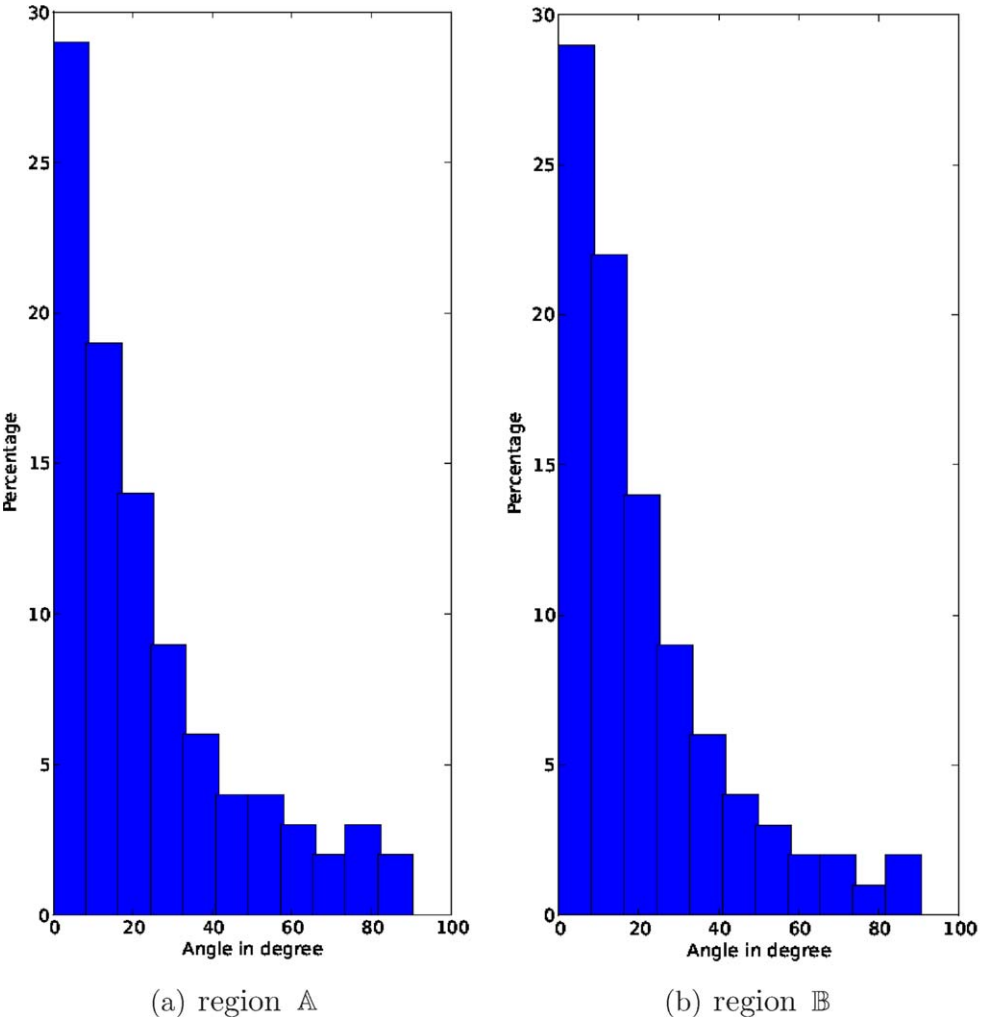

Figure 10. Histograms of angles (in degree) between the structure in the FSLE and the one in the SSS image on the study date, for (a) region $\mathbb{A}$ and (b) region $\mathbb{B}$.

As the inversion of FSLE is a success, the next step is to test several kinds of experiments to assess the inversion of tracers.

5.3. Minimizing the Cost Function

To illustrate the performance of the inversion algorithm, the evolution of the cost function and of the remaining error in the velocity field are computed for all experiments in both regions (Figure 11, where the iteration axis is logarithmic to improve the representation of the decreasing of the cost function and error). The behavior of the cost function is helpful to adjust simulated annealing parameters. As much as possible, information on the remaining error in the velocity field is not used to tune parameters of the inversion. The error on the velocity field, $\epsilon(\mathbf{u})$, represents the percentage of the norm of the error still present in the velocity $\mathbf{u}$ compared to the norm of the error on the background velocity:

$$\epsilon(\mathbf{u}) = \frac{||\mathbf{u} - \mathbf{u}_{true}||}{||\mathbf{u}_{background} - \mathbf{u}_{true}||} \tag{8}$$

The performance of the inversion in region $\mathbb{A}$ strongly depends on the tracer used for the inversion. In Figure 11a, the cost function decreases more efficiently in experiments 3 (inversion of SST and SSS images together, green line) and 4 (inversion of spiciness image, cyan line) than in experiments 1 and 2 where only one tracer

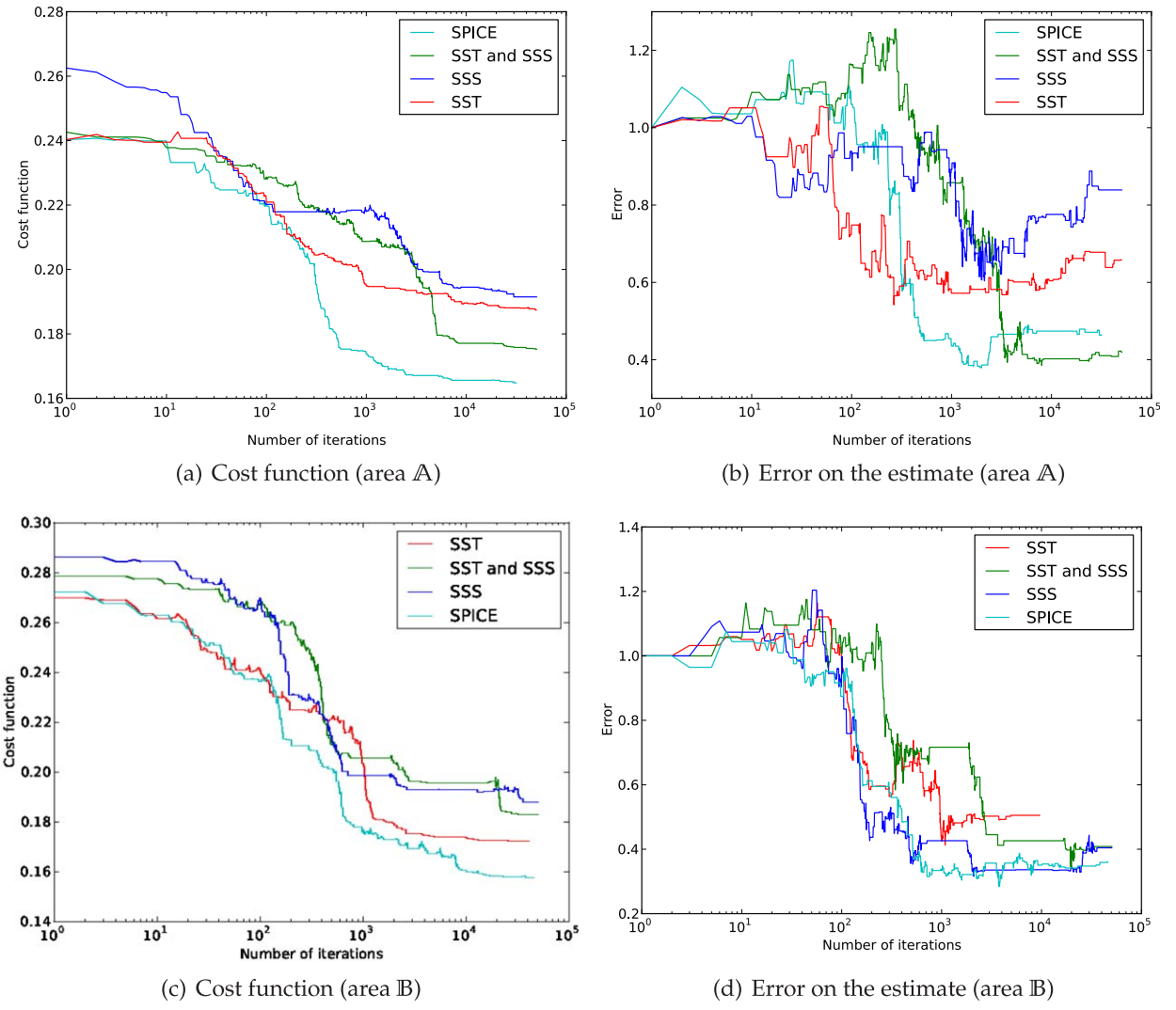

Figure 11. Evolution of the (a, c) cost function and (b, d) error on the velocity as a function of the number of iterations for four experiments.

is used (either SST in experiment 1 (red line) or SSS in experiment 2 (blue line)). Similarly, in Figure 11b, the error on the final estimated velocity is smaller in experiments 3 and 4 than in experiments 1 and 2.

The different behaviors and performances associated to the four experiments in region 𝔸 highlight the importance of using two kinds of different, complementary observations such as SST and SSS to perform the inversion. In this region, the smallest correction is obtained when the inversion is based on the SSS image alone. This means that the dynamical structures in this image are only partially extracted in region 𝔸 (Figure 4e). The inversion method clearly performs better when the spiciness image is used with a reduction of the background error larger than 60%. Two main reasons can explain the better performance of the inversion method with the spiciness image. First, this image contains richer information since spiciness is a linear combination of the complementary SST and SSS tracers. As region 𝔸 is very energetic, and the circulation quite complex, the use of both the SSS and SST tracers is necessary to reach a substantial reduction of the background error. Second, spiciness is a more dynamically passive tracer than SST and SSS alone, thus providing more useful information.

Results of the relative performances of the inversion method with different tracers are different in region 𝔹 (Figures 11c and 11d). In this region where tracers are likely passive and their binarized images more alike, the decrease of the cost function (Figure 11c) and of the error on the corrected velocity (Figure 11d) are

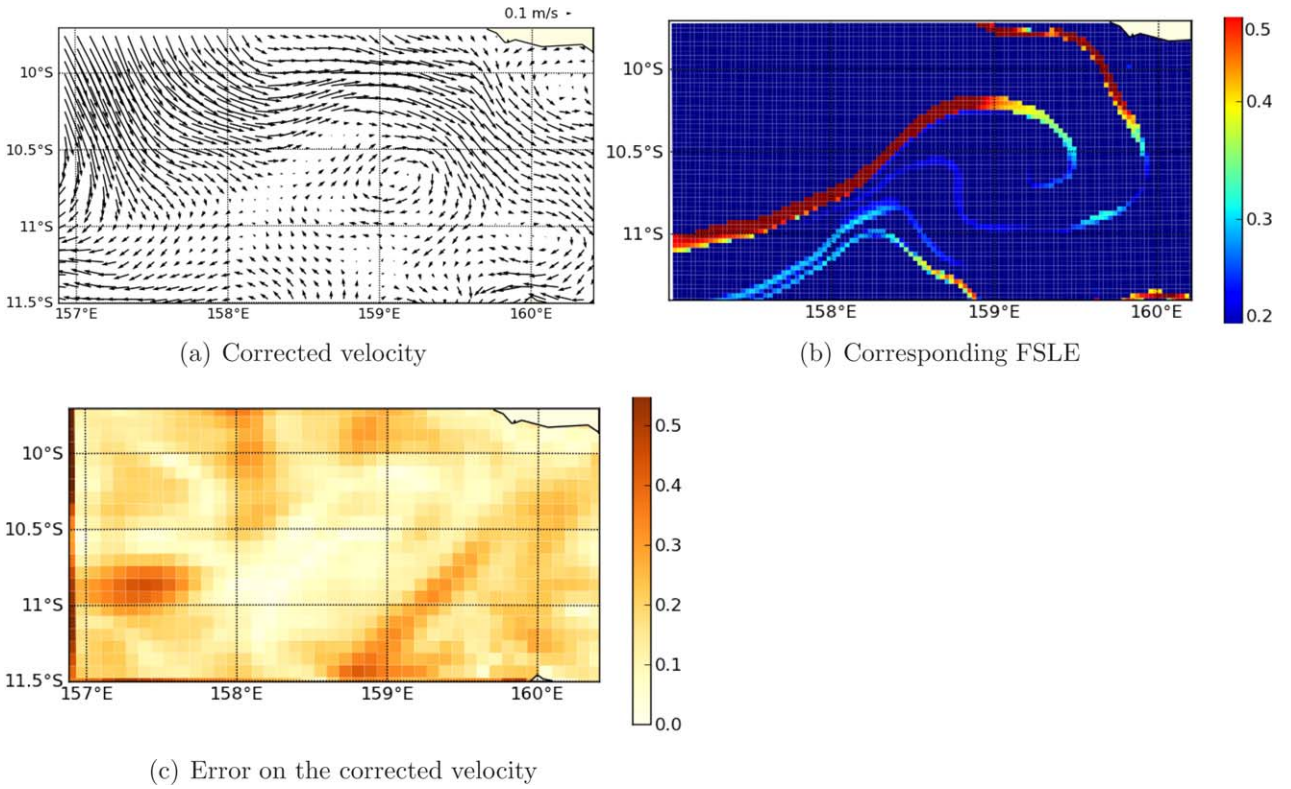

Figure 12. Results of the inversion of the SSS image in region $\mathbb{B}$. (a) Estimate of the velocity in ms^{-1}, (b) corresponding FSLE in days and (c) error on the estimate in ms^{-1}.

more similar for all experiments compared to region $\mathbb{A}$. The use of the SSS image alone enables to correct more than 60% of the error on the background velocity. The use of two tracers (experiment 3) does not improve the estimation of the circulation. However, the inversion of the SST tracer alone is not as efficient as the inversion of the SSS alone. It may be due to some undetected gradients in the northeastern part of the image $\mathcal{I}_{SST}$ (Figure 5c). The convergence of the cost function is a bit faster in experiment 4 (inversion of the spiciness) than in the other experiments, though the resulting accuracy of the estimated velocity is quite similar to what is obtained from the inversion of SSS alone or SST and SSS together.

In our test region $\mathbb{B}$, the use of both SST and SSS in the inversion is not really useful because the two sources of information are mostly redundant. The inversion of SSS alone is sufficient to reduce the error on the background velocity and to obtain a good convergence of the cost function.

The study of the inversion on two regions with various dynamics is striking since it shows different performances of the inversion process. For this reason, the choice of the tracer matters. In the following, only the inversion of the SSS image is shown in region $\mathbb{B}$, since all other experiments provide similar results. In region $\mathbb{A}$, however, the three following inversions will be discussed: inversion of SST alone, inversion of SSS alone and inversion of both tracers together. In this way, the contribution of each tracer on the estimation of the circulation can be assessed.

5.4. Estimated Velocities

To check the relevance of the optimally corrected velocity provided by the different inversion experiments, a closer examination of the estimated velocity is given in this section.

In region $\mathbb{B}$, the FSLE derived from the optimally corrected velocity (Figure 12b) is quite similar to the FSLE derived from the true velocity (Figure 9a). Moreover, the estimated structures are in better agreement with the structures detected in the tracer images. For instance, the position of the main eddy in the corrected velocity (Figure 12a) is in better agreement with the position of the same eddy in the tracer images. This is consistent with the strong reduction of velocity error as illustrated in Figure 12c. Therefore, the dynamical structures contained in the tracer image have proved to be useful to improve the estimation of the velocity in region $\mathbb{B}$.

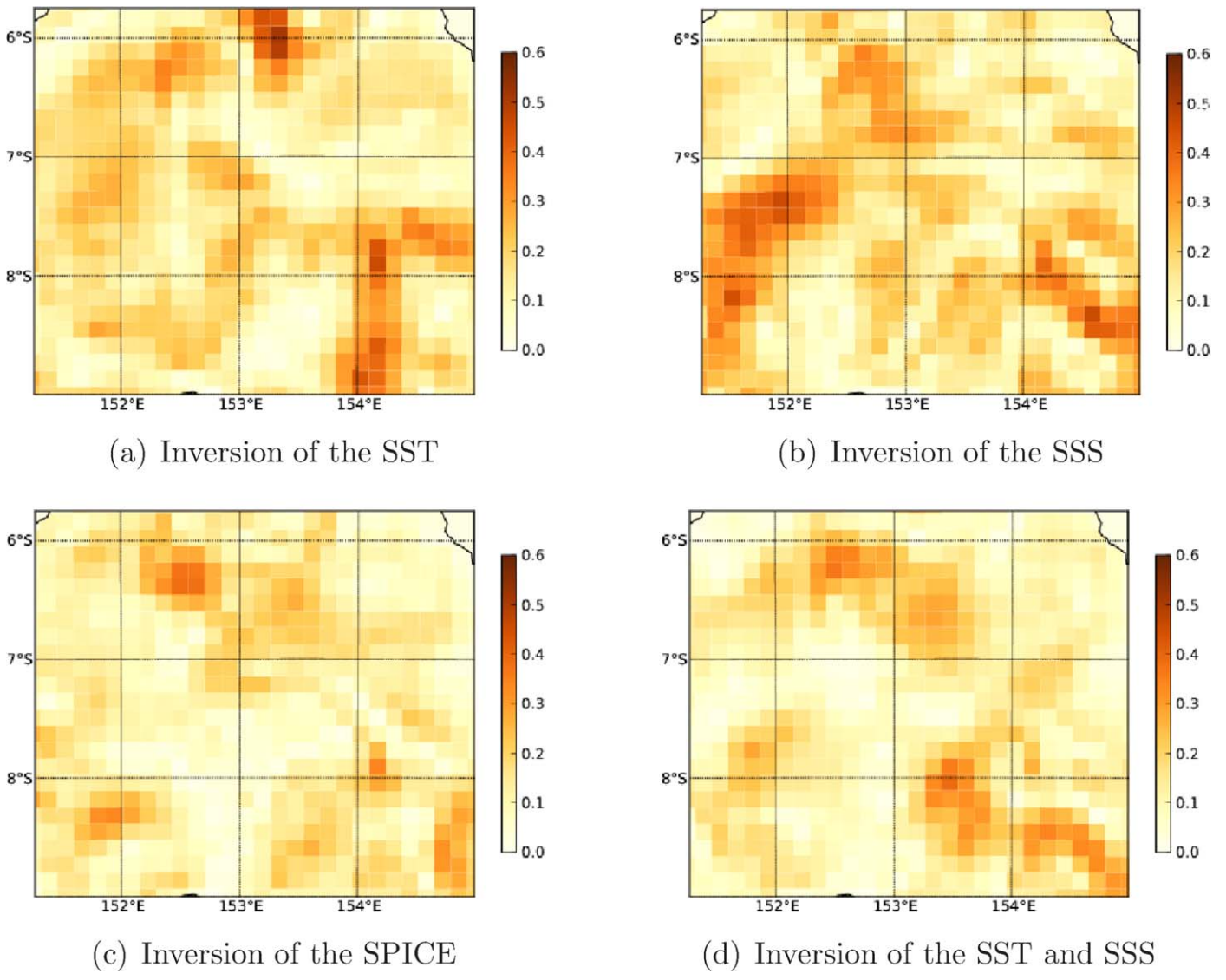

Figure 13. Error on the estimate in ms^{-1} in region $\mathbb{A}$ for the inversion of the (a) SST image alone, (b) SSS image alone, (c) SPICE image alone, and (d) inversion of the SST and the SSS images together.

In region $\mathbb{A}$, the different experiments show that tracers always add information to the background velocity. Errors in the corrected velocity field are increasingly reduced when more tracers are used in the inversion process (Figures 11a and 11b). This means that SST, SSS and spiciness contain different pieces of information on the dynamics in this region, and the detection of the frontal structures is therefore different and complementary in these images (see Figures 4c–4e). Yet the amplitude of the correction depends on the tracer used by the inversion.

Figure 13 represents the remaining error on the estimation of currents, namely the norm of the difference between the true velocity and the corrected velocity, for the four experiments. Comparing the corrections from the SST image alone (Figure 13a) and from the SSS image alone (Figure 13b), it can be seen that the major improvements are located in different areas for the inversion of these two tracers. Corrections based on SSS are mainly located in the northern part of the region, whereas corrections based on SST are mainly located in the western part of the region. This supports the idea that the dynamical information extracted from SST and SSS are complementary. Indeed, in the last two experiments, a substantial improvement is obtained when information from both SST and SSS are used, as compared to the inversion of one of these tracers alone (Figure 13d). The two images allow to obtain more relevant information than one single image, because some filaments detected in these images differ. As the spiciness tracer is built as a linear

combination of SST and SSS, this quantity also contains information from both tracer. Therefore the results of the inversion of the spiciness image are as good as if the two tracers are used separately in the cost function (experiment 4). Using several sources of information notably increases the amplitude of the correction.

6. Conclusion

The inversion of tracers consist in improving the estimation of the circulation by reducing the distance between two images of the same flow. One image is extracted from the FSLE (derived from the velocity), and the other one is constructed from the normalized gradient of the tracer. In this paper, a high-resolution model of the Solomon Sea has been proved to be a suitable laboratory to test the feasibility of the inversion of tracers. The model is quite realistic and the link between tracers (SST and SSS) and dynamics is reliable and representative of the real ocean. The model also provides quite a faithful representation of many submesoscale processes and simulated SST and SSS patterns are similar to what is detected in high-resolution satellite observations.

The process of inversion is then evaluated using synthetic observations of SST, SSS and velocity derived from the model simulation. This defines twin experiments, in which a perturbed velocity (to simulate background errors) has been corrected using tracer synthetic observation, and then compared with the true velocity. The estimation is performed by minimizing the distance between the frontal structures detected in the tracer image and the FSLE proxy, which corresponds to the image of the flow.

The analysis of the model shows that there is a good match between the FSLE derived from the true velocity and the frontal structure of the tracers so that the FSLE is a relevant proxy for the inversion.

The various inversion experiments of different tracers show that the information contained in the tracers are relevant to improve the evaluation of the dynamics. However, the performance of the inversion depends on the ability of algorithms to extract frontal structures from the tracer images. In this model, in the area where the bathymetry is complex and the dynamics is energetic (area $\mathbb{A}$), filaments are not very well detected in tracer images and the corresponding binarized images of the SST and the SSS contain contrasting information on the dynamics. In that case, the combined inversion of two tracers really helps the convergence of the cost function and the estimation of a more accurate velocity. The inversion of the image of the spiciness, which is a linear combination of SST and SSS, also gives more accurate results than the inversion of the SST alone or the SSS alone. In the other area (area $\mathbb{B}$), not as eddy-active as the previous one, the frontal structures are very well detected in both the SST and the SSS. Therefore, the use of one tracer (the SST or the SSS) is sufficient to correct the dynamics.

The feasibility of the inversion of tracer images to improve the circulation has been demonstrated using a realistic regional model and comforts the results found in G2013. However, in the more general perspective of data assimilation problems, some elements of the method may need to be revised. The main challenges are the constraint on the parameterization of the uncertainties in the background error covariance matrix, where a lot of statistical information is assumed to be known in this study, and the efficiency of the minimization of the cost function, which requires many iterations to reach the solution. The method has not yet been optimized and the slow decrease of the cost function may be challenging if one considers the whole domain of the Solomon Sea for data assimilation. Also, the method has been tested in cases where there is a good similarity between FSLE and tracer. The inversion of tracers using FSLE as a proxy may not be possible in other cases where stretching is not dominant in the fluid [*Lapeyre*, 2002]. FSLE structures may differ from tracer gradients if other physical processes such as surface forcing or strong vertical exchanges are present. One may think of alternative proxy such as singularity exponents [*Turiel et al*., 2005; *Isern-Fontanet et al*., 2007] and use them to compare an image of singular exponents computed from SSH with images of singular exponents computed from tracers.

Acknowledgments
This research has been conducted with the support of the CNES (French Space Agency) and the CNRS (French National Research center). Numerical simulations and inversions have been performed on IBM parallel supercomputer at the French IDRIS/CNRS computing center.

References

Aurell, E., G. Boffetta, A. Crisanti, G. Paladin, and A. Vulpiani (1997), Predictability in the large: An extension of the concept of Lyapunov exponent, *J. Phys. A Math. Gen.*, *30*(3), 4.

Blanke, B., and P. Delecluse (1993), Variability of the tropical Atlantic Ocean simulated by a general circulation model with two different mixed-layer physics, *J. Phys. Oceanogr.*, *23*(7), 1363–1388.

Capet, X., J. C. McWilliams, M. J. Molemaker, and A. F. Shchepetkin (2008a), Mesoscale to submesoscale transition in the California current system. Part I: Flow structure, eddy flux, and observational tests, *Am. Meteorol. Soc.*, *38*(1), 29–43.
Capet, X., J. C. McWilliams, M. J. Molemaker, and A. F. Shchepetkin (2008b), Mesoscale to submesoscale transition in the California current system. Part II: Frontal processes, *Am. Meteorol. Soc.*, *38*(1), 44–64.
Capet, X., P. Klein, B. L. Hua, G. Lapeyre, and J. C. McWilliams (2008c), Surface kinetic energy transfer in surface quasi-geostrophic flows, *J. Fluid Mech.*, *604*, 165–174.
Casella, G., and E. I. George (1992), Explaining the Gibbs sampler, *Am. Stat.*, *46*(3), 167–174.
Chelton, D. B., R. A. DeSzoeke, M. G. Schlax and K. El Naggar and N. Siwertz (1998), Geographical variability of the first baroclinic Rossby radius of deformation., *J. Geophys. Oceanogr.*, *28*, 433–460.
Cravatte, S., A. Ganachaud, Q.-P. Duong, W. S. Kessler, G. Eldin, and P. Dutrieux (2011), Observed circulation in the Solomon Sea from SADCP data, *Prog. Oceanogr.*, *88*, 116–130.
Debreu, L., C. Vouland, and E. Blayo (2008), AGRIF: Adaptive grid refinement in Fortran, *Comput. Geosci.*, *34*, 8–13.
Dee, D. P. (2011), The ERA-interim reanalysis: Configuration and performance of the data assimilation system, *Q. J. R. Meteorol. Soc.*, *137*(656), 553–597.
Djath, B., A. Melet, J. Verron, J. M. Molines, B. Barnier, L. Gourdeau, and L. Debreu (2014), A 1/36° model of the Solomon Sea embedded into a global ocean model: on the setting up of an interactive open boundary condition nested model system, *J. Oper. Oceanogr.*, *7*(1), 34–46.
d'Ovidio, F., V. Fernández, E. Hernández-García, and C. López (2004), Mixing structures in the Mediterranean Sea from finite-size Lyapunov exponents, *Geophys. Res. Lett.*, *31*, L17203, doi:10.1029/2004GL020328.
d'Ovidio, F., J. Isern-Fontanet, C. López, E. Hernández-García, and E. García-Ladona (2009), Comparison between Eulerian diagnostics and finite-size Lyapunov exponents computed from altimetry in the Algerian basin, *Deep Sea Res., Part I*, *56*(1), 15–31.
Ganachaud A., et al. (2007), Southwest Pacific Ocean Circulation and Climate Experiment (SPICE)—Part I. Scientific Background. International CLIVAR Project Office, CLIVAR Publication Series No. 111, *NOAA OAR Special Report*, pp. 37, NOAA/OAR/PMEL, Seattle, Wash.
Ganachaud, A., et al. (2008), Southwest Pacific Ocean Circulation and Climate Experiment (SPICE)—Part II. Implementation Plan. International CLIVAR Project Office, CLIVAR Publication Series No. 133, *NOAA OAR Special Report*, 36 pp., NOAA/OAR/PMEL, Seattle, Wash.
Gaultier, L., J. Verron, J.-M. Brankart, O. Titaud, and P. Brasseur (2013), On the inversion of submesoscale tracer fields to estimate the surface ocean circulation, *J. Mar. Syst.*, *126*(0),33–42.
Geman, S., and D. Geman (1984), Stochastic relaxation, Gibbs distributions, and the Bayesian restoration of images, *IEEE Trans. Pattern Anal. Mach. Intel.*, *PAMI-6*(6), 721–741.
Gourdeau, L., J. Verron, A. Melet, W. Kessler, F. Marin, and B. Djath (2014), Exploring the mesoscale activity in the Solomon Sea: A complementary approach with a numerical model and altimetric data, *J. Geophys. Res. Oceans*., *119*, 2290–2311, doi:10.1002/2013JC009614.
Haller, G. (2011), A variational theory of hyperbolic Lagrangian coherent structures, *Physica D*, *240*(7), 574–598.
Haller, G. and G. Yuan (2000), Lagrangian coherent structures and mixing in two dimensional turbulence, *Physica D*, *147*(3–4), 352–370.
Hernàndez-Carrasco, I., C. Lòpez, E. Hernàndez-Garcìa, and A. Turiel (2011), How reliable are finite-size Lyapunov exponents for the assessment of ocean dynamics?, *Ocean Modell.*, *36*(3–4), 208–218.
Hristova, H. G., and W. S. Kessler (2011), Surface circulation in the Solomon Sea derived from Lagrangian drifter observations, *J. Phys. Oceanogr., 42*(3), 448–458.
IOC, IHO, and BODC (2003), *Centenary Edition of the GEBCO Digital Atlas* [CD-ROM], Intergov. Oceanogr. Comm. and the Int. Hydrogr. Organ., Gen. Bathymetric Chart of the Oceans, Br. Oceanogr. Data Cent., Liverpool, U. K.
Isern-Fontanet, J., A. Turiel, E. Garcia-Ladona and J. Font (2007), Microcanonical multifractal formalism: Application to the estimation of ocean surface velocities, *J. Geophys. Res.*, *112*, C05024, doi:10.1029/2006JC003878.
Klein, P., A.-M. Treguier, and B. L. Hua (1998), Three-dimensional stirring of thermohaline fronts, *J. Mar. Res.*, *56*, 589–612.
Klein, P., G. Lapeyre, G. Roullet, S. L. Gentil, and H. Sasaki (2011), Ocean turbulence at meso and submesoscales: Connection between surface and interior dynamics, *Geophys. Astrophys. Fluid Dyn. 105*(4-5), 421–437.
Lacorata, G., E. Aurell, and A. Vulpiani (2001), Drifters dispersion in the Adriatic Sea: Lagrangian data and chaotic model, *Ann. Geophys.*, *19*, 121–129.
Lapeyre, G. (2002), Characterization of finite-time Lyapunov exponents and vectors in two-dimensional turbulence, *Chaos Interdisciplinary J. Nonlinear Sci.*, *12*(3), 688–698.
Lapeyre, G. (2009), What vertical mode does the altimeter reflect? On the decomposition in baroclinic modes and on a surface-trapped mode, *J. Phys. Oceanogr.*, *39*, 2857–2874.
Large, W., and S. Yeager (2009), The global climatology of an interannually varying air-sea flux data set, *Clim. Dyn.*, *33*, 341–364.
Lehahn, Y., F. d'Ovidio, M. Lévy, and E. Heifetz (2007), Stirring of the northeast Atlantic spring bloom: A Lagrangian analysis based on multisatellite data, *J. Geophys. Res.*, *112*, C08005, doi:10.1029/2006JC003927.
Levitus, S., T. Boyer, M. Conkright, T. O. Brien, J. Antonov, C. Stephens, L. Stathoplos, D. Johnson, and R. Gelfeld (1998), World Ocean Database 1998: Volume 1: Introduction, Technical report NOAA Atlas NESDIS 18, 346 pp., U.S. Gov. Print. Off., Washington, D. C.
Lévy, M., P. Klein, and A.-M. Tréguier (2001), Impact of sub-mesoscale physics on production and subduction of phytoplankton in an oligotrophic regime, *J. Mar. Res.*, *59*(4), 535–565.
Lévy, M., R. Ferrari, P. Franks, A. Martin, and P. Rivière (2012), Bringing physics to life at the submesoscale, *Geophys. Res. Lett.*, *39*, L14602, doi:10.1029/2012GL052756.
Luo, Y., L. Rothstein, R. Zhang, and A. Busalacchi (2005), On the connection between South Pacific subtropical spiciness anomalies and decadal equatorial variability in an ocean general circulation model, *J. Geophys. Res.*, *110*, C10002, doi:10.1029/2004JC002655.
Madec, G. (2008), *NEMO Reference Manual, Ocean Dynamic Component: NEMO-OPA, Note du Pôle de modélisation*, p. 866, Inst. Pierre-Simon Laplace, France.
Marchesiello, P., J. C. McWilliams, and A. Shchepetkin (2003), Equilibrium structure and dynamics of the California current system, *J. Phys. Oceanogr.*, *33*(4), 753–783.
Marchesiello, P., X. Capet, C. Menkes, and S. C. Kennan (2011), Submesoscale dynamics in tropical instability waves, *Ocean Modell.*, *39*(1-2), 31–46.
Mathur, M., G. Haller, T. Peacock, J. E. Ruppert-Felsot, and H. L. Swinney (2007), Uncovering the Lagrangian skeleton of turbulence, *Phys. Rev. Lett.*, *98*(14), 144502.
Melet, A., L. Gourdeau, and J. Verron (2010b), Variability of the Solomon Sea circulation from altimetry sea level data, *Ocean Dyn.*, *60*(4), 883–900.

Melet, A., L. Gourdeau, J. Verron, and B. Djath (2013), Solomon sea circulation and water mass modifications: Response at ENSO timescales, *Ocean Dyn.*, *63*, 1–19.

Munk, W. H., B. A. Warren, and C. Wunsch (1981), Internal waves and small-scale processes, in *Evolution of Physical Oceanography*, edited by B. A. Warren and C. Wunsch, chap. 9, pp. 264–291, MIT Press, Cambridge, Mass.

Nonaka, M., and S. Xie (2000), Propagation of North Pacific interdecadal subsurface temperature anomalies in an ocean GCM, *Geophys. Res. Lett.*, *27*, 3747–3750.

Pierrehumbert, R. T., I. M. Held, and K. L. Swanson (1994), Spectra of local and nonlocal two-dimensional turbulence, *Chaos Solitons Fractals*, *4*, 1111–1116.

Sasaki, H., and P. Klein (2012), SSH Wavenumber spectra in the North Pacific from a high-resolution realistic simulation, *J. Phys. Oceanogr.*, *42*, 1233–1241.

Shadden, S. C., F. Lekien, and J. E. Marsden (2005), Definition and properties of Lagrangian coherent structures from finite-time Lyapunov exponents in two-dimensional aperiodic flows, *Physica D*, *212*(3–4), 271 – 304.

Skamarock, W. C. (2004), Evaluating mesoscale NWP models using kinetic energy spectra, *Am. Meteorol. Soc.*, *132*, 3019–30,132.

Thomas, L. N., A. Tandon, and A. Mahadevan (2008), Submesoscale processes and dynamics, in *Ocean Modeling in an Eddying Regime, Geophys. Monogr. Ser.*, vol. 177, edited by M. W. Hecht and H. Hasumi, pp. 17–38, AGU, Washington, D. C.

Titaud, O., J. Brankart, and J. Verron (2011), On the use of finite-time Lyapunov exponents and vectors for direct assimilation of tracer images into ocean models, *Tellus, Ser. A.*, *63*(5), 1038–1051.

Tréguier, A. M., B. Barnier, A. P. de Miranda, J. M. Molines, N. Grima, M. Imbard, G. Madec, C. Messager, T. Reynaud, and S. Michel (2001), An eddy-permitting model of the Atlantic circulation: Evaluating open boundary conditions, *J. Geophys. Res.*, *106*, 22,115–22,129.

Turiel, A., J. Isern-Fontanet, E. Garcia-Ladona and J. Font (2005), Multifractal method for the instantaneous evaluation of the stream function in geophysical flows, *Phys. Rev. Lett.*, *95*, 104502.

Van Laarhoven, P., and E. Aarts (1987), *Simulated Annealing: Theory and Application*, Kluwer Acad., Dordrecht, Netherlands.

Veronis, G. (1972), On properties of seawater defined by temperature, salinity, and pressure, *J. Mar. Res.*, *30*, 227–255.

Yeager, S. G., and W. G. Large (2004), Late-winter generation of spiciness on subducted isopycnals, *J. Phys. Oceanogr.*, *34*, 1528–1545.